NAM

The influence of stress rates on induced seismicity rates within the Groningen gas field

Seismological Model

Shell Research

Stephen Bourne and Steve Oates

Date October 2018

Editors Jan van Elk & Dirk Doornhof

General Introduction

The seismological model (Version 5) currently used in the assessment of hazard and risk for the induced seismicity in Groningen, provides a probabilistic prediction of the seismicity dependent on the local reservoir pressure depletion associated with the gas volume produced. The seismicity is in this model not dependent on the gas production rate. The gas volume extracted determines reservoir pressure depletion, which governs the expected number and magnitude of induced earthquakes. Within the model, the expected number of events depends on the pressure depletion, but not the rate of that depletion. Theoretically, there are processes which potentially could cause the expected event number, for a given incremental volume of gas production to depend on the rate of that gas production. These could be associated with the geomechanical behaviour of faults (e.g. rate and state frictional fault behaviour) or compaction (e.g. a-seismic stress relaxation at production time scales).

However, studies carried out as part of the research program of NAM have not been able to identify whether these processes play a significant role or been able to quantify the impact of gas production rate on seismicity. In an environment of decreasing and more stable gas production rates, ignoring potential production rate dependency of the seismicity will be conservative and lead to a potential over-estimation of hazard and risk.

Given the current state of knowledge, NAM is not in a position to increase the sensitivity of the seismological model to production rate changes as this was so far found to degrade the performance of the model and accepts that as a result the assessment of hazard and risk might be conservative. The current model yields a sensitivity to seasonal depletion rate changes that is thought to be close to the upper bound of sensitivities consistent with the observed catalogue. On the other hand, based on the research to date, seasonal seismicity variations within the catalogue are lower than the detection threshold.

In the operation of the field, NAM will make every effort to reduce fluctuations in gas production. The Minister of Economic Affairs has, on the advice of the regulator SodM, imposed limits to the production fluctuations. NAM will report on any excursions from these set limits.

In recent years, NAM has carried out several studies into the dependency of the induced seismicity in Groningen on the gas production rate from the field. This included studies into reservoir behaviour (Ref. 1), modelling of the various mechanisms that could induce production rate dependency (Ref. 4) and analysis of field data using machine-learning (Ref. 6) and statistical techniques (Ref. 2, 3 and 5).

This report consists of two sections. The first investigates evidence for periodicity in the earthquake record using statistical techniques. This is followed by an extension of the seismological model (version 5) (Ref. 7 and 8) to include physical mechanisms leading to stress relaxation like poro-visco-elastic stresses that could account for production rate dependency of induced seismicity in the Groningen field.

References

1. Geurtsen, L., P. Valvatne and A. Mar-Or, Optimisation of the Production Distribution over the Groningen field to reduce Seismicity, NAM, December 2017
2. Bierman S.M., R. Paleja, and M. Jones, Statistical methodology for investigating seasonal variation in rates of earthquake occurrence in the Groningen field, January 2016
3. Bierman S.M., Seasonal variation in rates of earthquake occurrences in the Groningen field, August 2017
4. DeDontney, Nora, and Suvrat Lele, Impact of Production Fluctuations on Groningen Seismicity – Part 1, Geomechanical Modelling using Rate of State friction, ExxonMobil Upstream Research Company, 2018.
5. Burch D. and B. Symington, Impact of Production Fluctuations on Groningen Seismicity – Part 2, Data Analytics, ExxonMobil Upstream Research Company, 2018.
6. Park T., H. Jamali-Rad, W. Oosterbosch, J. Limbeck, F. Lanz, C. Harris, E. Barbaro, K. Bisdom & K. Nevenzeel, Seasonality analysis for induced seismicity event rate time series within the Groningen Field, Shell Research and IBM, August 2018.
7. Bourne, S.J., Oates, S.J., 2017. Extreme threshold failures within a heterogeneous elastic thin-sheet and the spatial-temporal development of induced seismicity within the Groningen gas _eld. Journal of Geophysical Research: Solid Earth 122, 10,299{10,320.
8. Bourne, S.J., Oates, S.J., Elk, J.V., 2018. The exponential rise of induced seismicity with increasing stress levels in the Groningen gasfield and its implications for controlling seismic risk. Geophysical Journal International 213, 1693-1700.

NAM

Title	**The influence of stress rates on induced seismicity rates within the Groningen gas field - Seismological Model**		**Date**	October 2018
			Initiator	NAM
Autor(s)	**Stephen Bourne and Steve Oates**	**Editors**	Jan van Elk and Dirk Doornhof	
Organisation	Shell Research	**Organisation**	NAM	
Place in the Study and Data Acquisition Plan	Study Theme: Impact Production Fluctuations Comment: The seismological model (Version 5) currently used in the assessment of hazard and risk for the induced seismicity in Groningen, provides a probabilistic prediction of the seismicity dependent on the local reservoir pressure depletion associated with the gas volume produced. The seismicity is in this model not dependent on the gas production rate. The gas volume extracted determines reservoir pressure depletion which governs the expected number and magnitude of induced earthquakes. Within the model, the expected number of events depends on the pressure depletion but not the rate of that depletion. Theoretically, there are processes which potentially could cause the expected event number for a given incremental volume of gas production to depend on the rate of that gas production. These could be associated with the geomechanical behaviour of fault (e.g. rate and state frictional fault behaviour) or compaction (e.g. a-seismic stress relaxation at production time scales). However, studies carried out as part of the research program of NAM have not been able to identify whether these processes play a significant role or been able to quantify the impact of gas production rate on seismicity. In an environment of decreasing and more stable gas production rates, ignoring potential production rate dependency of the seismicity will be conservative and lead to a potential over-estimation of hazard and risk. Given the current state of knowledge, NAM is not in a position to increase the sensitivity of the seismological model to production rate changes as this was so far found to degrade the performance of the model and accepts that as a result to assessment of hazard and risk might be conservative. The current model yields a sensitivity to seasonal depletion rate changes that is thought to be close to the upper bound of sensitivities consistent with the observed catalogue. On the other hand, the effect is, based on the research to date, seasonal seismicity variations within the catalogue are less than the detection threshold. In the operation of the field, NAM will make every effort to reduce fluctuations in gas production. The Minister of Economic Affairs has, on the advice of the regulator SodM,			

	imposed limits to the production fluctuations. NAM will report on any excursions from these set limits. In recent years, NAM has carried out several studies into the dependency of the induced seismicity in Groningen on the gas production rate from the field. This included studies into reservoir behaviour, modelling of the various mechanisms that could induce production rate dependency and analysis of field data using machine-learning and statistical techniques. This report consists of two sections. The first investigates evidence for periodicity in the earthquake record using statistical techniques. This is followed by an extension of the seismological model (version 5) to include physical mechanisms leading to stress relaxation like poro-visco-elastic stresses that could account for production rate dependency of induced seismicity in the Groningen field.
Directliy linked research	(1) Gas Production (2) Reservoir Modelling (3) Geomechanical Modelling (4) Seismological Model
Used data	KNMI Earthquake catalogue Groningen gas production data
Associated organisation	NAM
Assurance	

The influence of stress rates on induced seismicity rates within the Groningen gas field

S.J. Bourne, S.J. Oates

29 August, 2018

Abstract

Seismicity induced by natural gas production from the Groningen field in the northeast of the Netherlands occurs on faults exposed to significant seasonal and secular variations in pore pressure depletion rates. Under these conditions, transient seismicity rate variations on Coulomb frictional faults embedded in a linear, poro-elastic reservoir would be proportional to and instantaneous with pressure depletion rate variations. In comparison, a poro-visco-elastic reservoir would allow some degree of aseismic stress relaxation over a characteristic time-scale meaning induced seismicity response would exhibit some time-delay and greater sensitivity to depletion-rate variation. Alternatively, relative to Coulomb friction, rate and state frictional fault behaviour would delay and modify induced seismicity rate responses to depletion-rate variations.

By extension of an existing elastic thin-sheet, Coulomb friction model of induced seismicity (Bourne and Oates, 2017) we find no evidence for any improvement in model performance by including viscoelasticity or rate and state friction. The observed small amplitude and time-scale of induced seismicity rate responses to large seasonal and secular stress rate variations reveals the likely limited influence of creep mechanisms, such as viscoelasticity or rate and state friction. If active, these creep mechanisms would allow some aseismic relaxation of depletion-induced stresses meaning lower depletion rates would avoid rather than only delay some induced seismicity relative to the same depletion achieved at a higher rate. Our results show no significant evidence of such creep mechanisms, but instead support elastic and Coulomb friction limits on the amplitude of expected near-instantaneous induced seismicity rate responses to future gas production policy changes.

1 Introduction

The influence of stress rates on induced seismicity is of general interest in relation to controlling the associated seismic hazard and risk. For the Groningen gas field in the Netherlands this is of particular importance since gas production rates are being decreased as part of measures to ensure safety for the exposed population. Pore pressure depletion within a linear poroelastic reservoir increases both the fault-normal effective stress and the fault-parallel shear stress. The first increases frictional resistance to inhibit fault slip, whilst the second promotes fault slip in a normal-faulting manner. The balance between these competing effects depends on geometric, elastic and frictional properties (Bourne and Oates, 2017) such that fault stability may increase or decrease with pressure depletion according to local conditions.

For Coulomb friction faults destabilized by pressure depletion, the resulting rates of induced seismicity respond instantly and in proportion to any changes in stress rate. This means the expected number of induced earthquakes depends on the incremental stress and not on the average rate or time-history of that stress increment. Consequently, within a Coulomb friction system, decreased stress rates cause decreased seismicity rates simply by spreading the same expected number of earthquakes over a longer time interval. There are of course other possible mechanisms for stress relaxation in addition to seismogenic fault slip. Dislocation creep, pressure dissolution, grain boundary creep, and time-dependent cracking are all possible mechanisms for stress rate dependent aseismic stress relaxation within the reservoir. Likewise, slip and slip-rate dependent evolution of frictional resistance creates scope for stress rate dependent aseismic fault slip.

If depletion rates are sufficiently small then aseismic stress relaxation rates may be sufficient to accommodate poroelastic stress build-up rates thereby avoiding any further stress build-up or induced seismicity. For increasing depletion rates, poroelastic stress rates will eventually out-pace aseismic relaxation rates so that seismicity rates increase to accommodate the entire elastic stress build-up rate. Gas production rates from the Groningen field have varied significantly from winter to summer and from year to year according to market demand. Since 2013, production rates and its variations were significantly reduced in response to increasing rates of induced seismicity. Given these significant seasonal and secular changes in depletion rates, there are opportunities to characterise these potential creep mechanisms according to the observed temporal relationship between depletion rate and induced seismicity rate variations. The purpose of this paper is to describe the field evidence for any stress rate dependent creep effects influencing induced seismicity rates within the Groningen gas field.

There are three key time-scales of response to variations in gas production rate:

1. Time-scale of pore pressure diffusion within the reservoir to gas production rates from wells,

2. Time-scale of reservoir deformation response to changes in pore pressure depletion,

3. Time-scale of frictional failure response to changes in reservoir deformation.

Throughout this analysis, we use the existing NAM reservoir pressure model as a complete description of the first time-scale that varies spatial according to reservoir properties. This is a model of 2-phase (water and gas) fluid transport through a porous medium driven by the measured time series of gas production from each production well. Properties of the porous medium are constrained directly by in-well petrophysical measurements and indirectly by reflection seismic imaging and in-well pressure measurements. This model provides a detailed, well-constrained, and physics-based description of the spatiotemporal evolution of reservoir pore pressures throughout the history of gas production and forecasts according to future production plans.

We will investigate the second time-scale by comparing the response for viscoelastic and elastic reservoir deformations with observed seismicity rate variations. Likewise, for the third time-scale we will compare the expected responses for rate and state fault friction with Coulomb friction. Our intent is to determine if the existing elastic Coulomb seismological model for the Groningen field (Bourne and Oates, 2017; Bourne et al., 2018) is appropriate given its instantaneous response time-scales - or if alternative seismological models based on viscoelasticty or rate and state friction perform better.

Several authors have previously explored induced seismicity under rate and state friction conditions using poroelastic, explicit fault models for fluid injection (Dieterich et al., 2015; Segall and Lu, 2015; Wenzel, 2015; Chang and Segall, 2016; Kroll et al., 2017), and fluid extraction (DeDontney and Lele, 2018; Dempsey and Suckale, 2017). Any comparisons with observed space-time evolution of induced seismicity rates were qualitative. This study uses Bayesian methods to estimate an ensemble of history-matched models and to measure the statistical significance of any differences in predictive performance.

2 Variations in pressure depletion rates

Natural gas production from the Groningen field and its associated reservoir pore pressure depletion began in 1963. The first instrumentally-recorded earthquake in the region was reported by the Royal Netherlands Meteorological Institute (KNMI) in 1986 (Dost et al., 2012). For the Groningen field earthquake catalogue, the magnitude of completeness for event detection and location is taken to be $M_L = 1.5$, starting in April 1995 (see Dost et al., 2012). Accordingly, we focus our analyses on the 289 $M_L \geq 1.5$ events reported by KNMI within the Groningen field between 1 April 1995 and 1 January 2018.

Over this period mean reservoir pressure decreased from 23 to 15 MPa, whilst mean annual depletion rates decreased from 0.35 MPa/year in 1995 to 0.25 MPa/year in 2004, increased to 0.45 MPa/year in 2013, and decreased again to 0.3 MPa/year before 2018 (Figure 1). Seasonal variations in gas production rates driven by summer-to-winter differences in the market demand created significant annual harmonic-like variations in mean depletion rates with a variable amplitude from 0.1 MPa/year in 2000 up to 0.2 MPa/year over the next decade. Following a 2015 change in production policy, seasonal fluctuations in mean depletion rates were essentially eliminated. The cor-

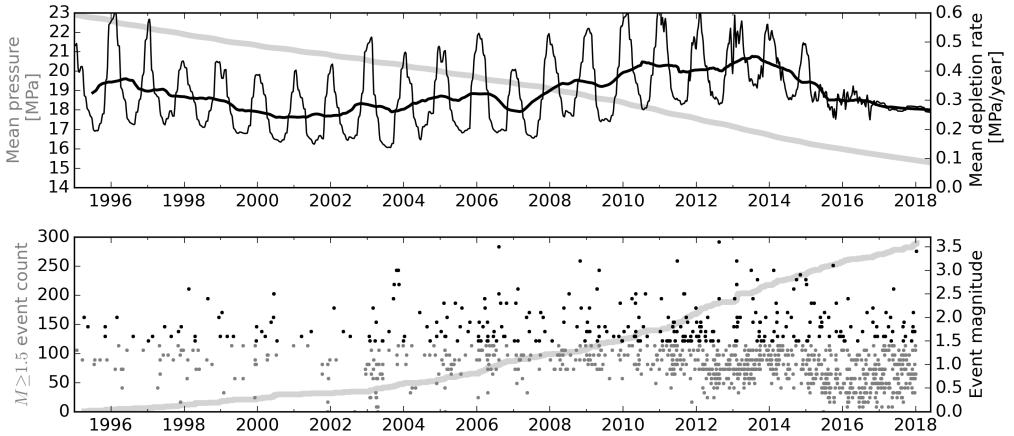

Figure 1: Time series of weekly mean reservoir pressure and the associated weekly and annual mean depletion rates. Reservoir grid blocks with less than 1 MPa depletion in 2018 are excluded as part of the non-depleting aquifer. Reservoir pressures are compared to the time series of cumulative $M \geq 1.5$ event counts and event magnitudes above and below the $M = 1.5$ magnitude of completeness denoted by black and grey dots respectively.

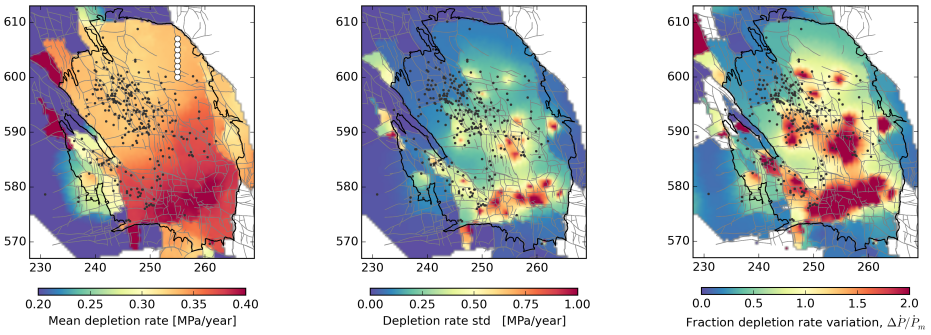

Figure 2: Mean depletion rates, $\dot{P}_m$, standard deviation in depletion rates, σ, and fractional variation in depletion rates, $\Delta\dot{P}/\dot{P}_m$ measured as $2\sigma/\dot{P}_m$. All quantities are for the interval from 1995 to 2018.

responding time series of reported earthquake occurrences and magnitudes (Figure 1) shows a generally increasing rate of induced seismicity with increasing depletion. The first half of the 7 MPa mean pressure depletion from 1995 to 2018 induced *c.* 100 $M \geq 1.5$ events in 13 years (1995–2008), whereas the second half induced nearly 200 $M \geq 1.5$ events in just 10 years (2008–2018). Is this doubling of earthquake nucleation rates per unit depletion due to a 30% increase in the mean depletion rate from 0.27 to 0.35 MPa/year? If so, this non-linear rate dependence could, in principle, be due to viscoelastic deformations where lower depletion rates allow more time for aseismic creep stress relaxation and a correspondingly smaller rate of earthquake nucleation per unit depletion. Alternatively, the increased rate of earthquakes per unit depletion may be a non-linear response to larger incremental shear stresses in the second depletion period. One such mechanism for this is a non-uniform, localised distribution of initial fault stresses, loaded by elastic reservoir deformations leading to initial exponential-like failure rates in the tail of the initial stress distribution (Bourne and Oates, 2017; Bourne et al., 2018).

The large seasonal and repeated variations in depletion rates over 21 cycles offers an opportunity to distinguish between these two possible physical mechanisms according to phase and amplitude response of induced seismicity to these harmonic variations. Relative to the multi-year secular trend in seismicity rate, there is some apparent shorter-term intra-year variability in rates that may relate to the 1995-2015 seasonal depletion rate fluctuations. However, given the limited number of observed events and their sparse distribution over so many cycles distributed, a detailed analysis is required to characterize and assess these effects.

There is good pressure communication throughout most of the reservoir

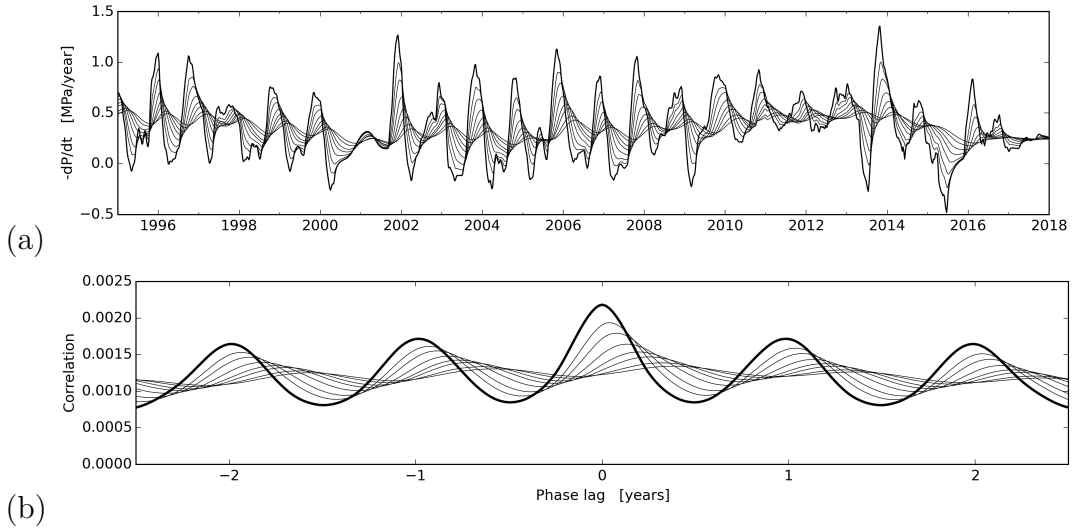

Figure 3: (a) Depletion rate time series at locations 1 km apart and spanning 0-7 km from a production well denoted by white circle in Figure 2. (b) Cross-correlations relative to the time series at the well location. Correlations decrease and phase lags increase with distance from the production well. Local correlation maxima occur for integer year phase lags due to the strong annual periodicity in depletion rate variations.

and spatial mean depletion rates are quite uniform with the largest rates in the south and southeast where most gas production occurs (Figure 2). The largest standard deviations in depletion rates are located around individual production well clusters and these fluctuations diminish with distance away from these production wells consistent with the hydraulic diffusion of pore pressure through the reservoir pore-space. Figure 3 shows a simple example of how pressure diffusion away from production wells diminishes the amplitude and increases the phase lag of depletion rate fluctuations with distance from a production well.

A map of these diffusion-controlled dominant time-lags in depletion rate fluctuations reveals significant spatial variation governed by the geographical distribution of production wells (Figure 4). This pattern result from the superposition of depletion rates time series associated with each production well and their associated amplitude decays and phase lags with distance. The dominant phase lags found at each location reflect the largest amplitudes typically associated with the shortest distance to a production well as all wells follow the seasonal variation on production rates with similar amplitudes and phases.

Earthquake epicentres occur across the range of observed time-lags from

0 to 120 days. In some places, phase-lags are not measured due to poor correlations largely associated with the absence of seasonal fluctuations. A notable example of this is the north-west region of seismicity separated from production wells by reservoir faults that act as pressure baffles that suppress seasonal fluctuations by effectively increasing the apparent diffusion length-scale. Clearly the local shear stresses that drive any seasonal variations in seismicity are not in-phase across the reservoir, but instead systematically vary with distance to the closest production well up to at least a quarter cycle (3 months). Consequently, any calendar month based assessment of seasonal seismicity variations will under-estimate the effect by stacking seismicity rates out-of-phase with depletion rate fluctuations. One simple solution is to assess periodicity using modified earthquake origin times obtained by subtracting the phase-lag at the epicenter from the observed origin time. Another solution is to incorporate these spatial-temporal variations in depletion rates into suitable seismological models and compare their performance with the observed earthquake catalogue. We will now describe results obtained from both approaches.

In some places the seasonal fluctuations are large enough to cause transient periods of increasing pore pressures that temporarily reverse a small part of the previous pressure depletion as indicated by the orange and red regions in the right-most map of Figure 2.

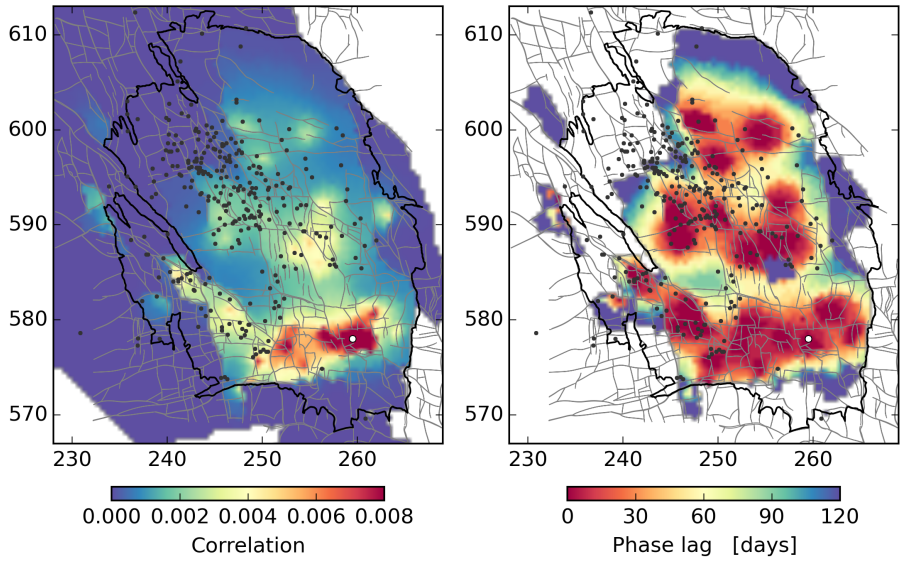

Figure 4: Correlation and phase lag of depletion rate time series relative to a reference location (white circle) selected with a large production well cluster. Black dots denote the 1995 to 2018 $M \geq 1.5$ earthquake epicentres.

3 Periodicity of induced seismicity rates

Several previous assessments of the Groningen earthquake catalogue for seasonal $M \geq 1.5$ event rate variations found no significant evidence for any measurable effect across a multiplicity of different methods and authors (Bierman et al., 2015, 2016; Nepveu et al., 2016; Pijpers, 2016; Bierman, 2017; Pijpers, 2018; Park et al., 2018). Where statistical significance was assessed, several authors found increasingly significant evidence for some seasonality within $M \geq M_{min}$ event rate variations for M_{min} decreasing from 1.5 to 1.0 (Bierman et al., 2015, 2016; Park et al., 2018). However, this is also accompanied with increasingly rates of diurnal variation where apparent night-time rates significantly exceed daytime rates (Bierman, 2017). Collectively, these findings indicate that apparent seasonality are most likely due to variations in the detection threshold for reporting earthquakes as the noise floor varies from day to night and summer to winter.

Here, we will reapply the Schuster test to the Groningen catalogue (Bierman, 2017) and focus on the detection threshold. We favour this method for its simplicity, long history of application to natural seismicity (Schuster, 1897; Heaton, 1975; Tanaka et al., 2002, 2006; Ader and Avouac, 2013) and tests of statistical significance given the limited catalogue size (Ader and Avouac, 2013). The Schuster test measures the probability, or p-value, that the frequency of event origin times, t within a catalogue varies as a harmonic function of time with period T. A phase angle for the i_{th} event is defined as $\theta_i = 2\pi t_t/T$, associated with the unit vector $\mathbf{d}_i = (\cos\theta_i, \sin\theta_i)$. The resultant phase vector from the 2D walk of all N phase vectors is calculated as

$$\mathbf{d} = \Sigma_{i=1}^{i=N} d_i, \tag{1}$$

and the total distance walked, $D = |\mathbf{d}|$, defines the probability of the null hypothesis that the origin times are uniformly distributed according to (Schuster, 1897)

$$p = e^{-D^2/N}. \tag{2}$$

Under this test, detectable periodicity in an earthquake catalogue yields a small Schuster p-value. However, a small Schuster p-values does not necessarily mean the seismicity rates are periodic at that time period. To overcome this ambiguity, Ader and Avouac (2013) proposed a statistical significance test for a spectrum of Schuster p-values evaluated at a restricted set of uncorrelated time-periods.

Following this procedure, Figure 5a shows the Schuster spectrum obtained for all $M \geq 1.5$ events within the Groningen catalogue since April 1995. Only

time periods in the range 190 to 200 days appear significant at the 95% confidence level. There is no evidence for annual periodocity associated with seasonal variations in the depletion induced stress rates or for lunar or diurnal time periods associated with earth tide induced stress rates. Allowing for the phase-lag in seasonal variations of reservoir stress rates due to pressure diffusion away from production wells, we also computed the Schuster spectrum for modified earthquake origin times. Modified origin times were computed by subtracting the epicentral diffusion time-lag (Figure 4) from the original origin time. This step corrects for the spatial pattern of depletion rate phase lags across the reservoir so that local depletion and seismicity rates are shifted to be in-phase with the seasonal variation in production rates. The resulting Schuster spectrum (Figure 5b) shows no time periods exceeding the 95% confidence limit. So for $M \geq 1.5$ events, we find that any annual periodicity within the catalogue is indistinguishable from a uniform random process.

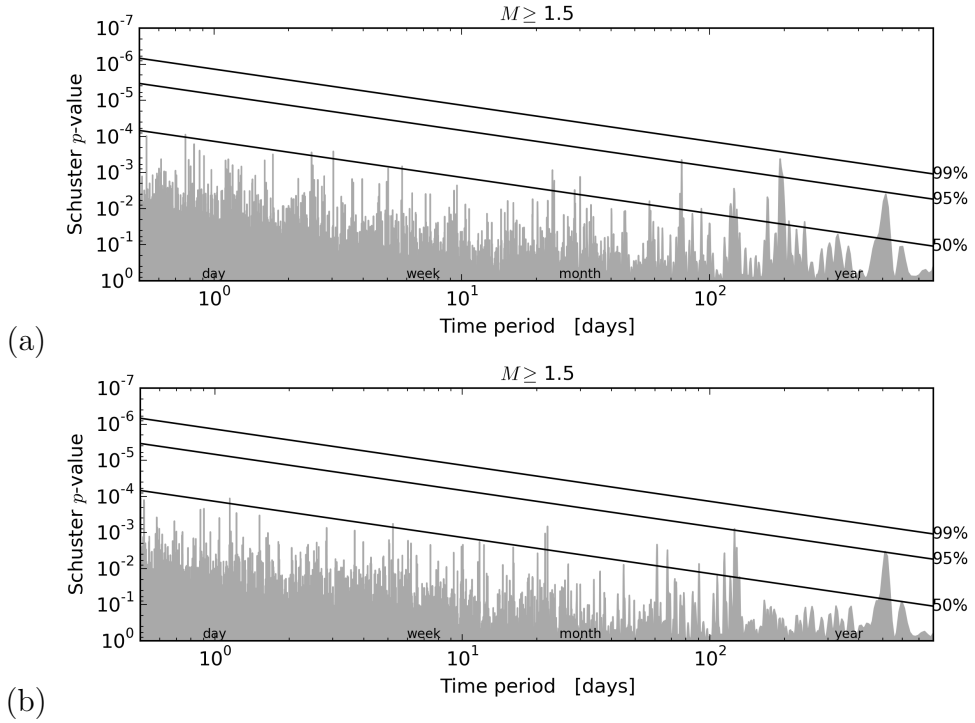

Figure 5: Schuster spectra of 1995-2015 $M \geq 1.5$ earthquakes according to (a) origin times as originally reported, and (b) origin times shifted according to the pressure phase-lag map shown in Figure 4. Thresholds of statistical significance are shown for 50, 95 and 99% confidence levels. For a one-year time period, both spectra indicate p-values below the 50% confidence level.

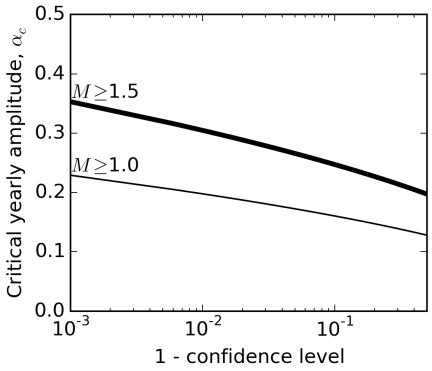

Figure 6: The smallest detectable relative amplitude in annual seismicity rate variations, α_c, according to confidence level for the Schuster test applied to the Groningen earthquake catalogue for $M \geq 1.5$ or $M \geq 1.0$ events.

The minimum detectable relative amplitude of periodic rate variations, α_c depends on catalogue size, N and the statistical confidence level, c. Modifying Ader and Avouac (2013) equation 10 for a general confidence level, c, we obtain (Appendix A)

$$\alpha_c = \frac{2}{\sqrt{N}} \sqrt{\log(t/T) - \log(1-c) - 1}, \tag{3}$$

where t is catalogue duration, and T is the time period of seismicity rate variations. Figure 6 shows this minimum amplitude of detection varies with confidence level for annual periodicity within the Groningen catalogue. At the 95% confidence level, the smallest detectable relative amplitudes of annual variability in seismicity rates, α_c, is 30% and 20% for $M \geq 1.5$, and $M \geq 1.0$ respectively.

Clearly, a lower M_{min} means greater detection sensitivity, but at the risk of bias due to incompleteness of detection for the smaller magnitudes. For $M_{min} \geq 1.5$, b-value estimates are stable within limits (Figure 7a), whereas for lower minimum magnitudes b-value estimates systematically and significantly decrease consistent with increasing detection bias. This indicates the magnitude of completeness, M_c since 1995 is $M_c = 1.5$.

Schuster's p-values obtained for $M \geq M_{min} | M_{min} \geq M_c$ events consistently indicate less than 50% confidence regarding annual periodicity in seismicity (Figure 7b). From (3), this implies $\alpha < 0.2$. In contrast, for $M_{min} < M_c$ Schuster's p-values for annual periodicity systematically and significantly increases with decreasing M_{min}. Together, this evidence clearly indicates any annual variations in induced seismicity rates are too small to

be detected within the available earthquake catalogue, whereas there is significant seasonal variation in event detection rates for small, $M \leq 1.5$, events below the magnitude of completeness for this network since 1995.

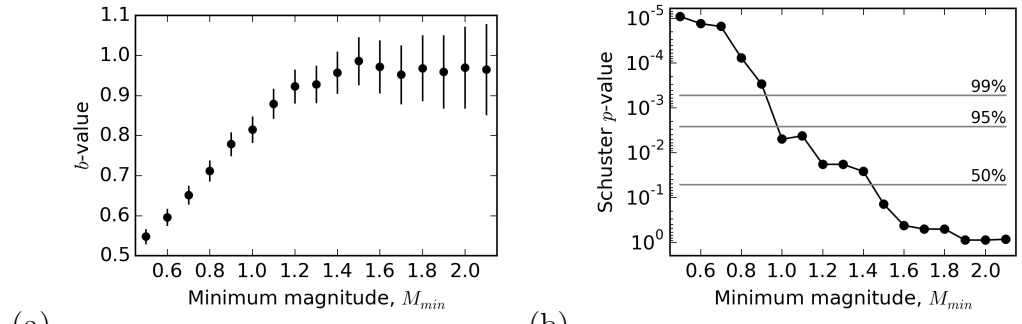

(a) (b)

Figure 7: Sensitivity of (a) maximum likelihood b-value estimates, and (b) Schuster p-value estimates to the minimum event magnitude threshold, M_{min}. For $M_{min} \geq 1.5$, b-value estimates are stable within limits and Schuster's p-values indicate less than 50% confidence in annual periodicity in seismicity. Error bars denote standard 1-sigma errors.

4 Elastic thin-sheet with Coulomb faults

Let us first consider the induced seismicity response expected for a linear elastic, thin-sheet reservoir embedded with Coulomb frictional faults. Elastic deformations represent an instantaneous and linear response of stress rates to depletion rate variations. Coulomb friction failures represent an instantaneous and linear response of seismicity rates to shear stress rate variations. The thin-sheet approximation allows simple analytic expressions for the deformation and failure processes within a heterogeneous reservoir avoiding the need for more complex and slower numerical models.

Deformations due to pore-pressure changes within a heterogeneous, faulted reservoir geometry that is laterally extensive relative to its thickness and depth below surface, are predominantly vertical and uni-axial. Within this thin-sheet approximation (Bourne and Oates, 2017), the vertically-averaged maximum Coulomb reservoir stress, C, is

$$\begin{aligned} C(\boldsymbol{x},t) &= C_i + \Delta C(\boldsymbol{x},t), \\ \Delta C(\boldsymbol{x},t) &= -\gamma\Gamma H \epsilon_{zz}, \end{aligned} \tag{4}$$

where $\boldsymbol{x}$ is the horizontal reservoir position vector, t is time, $\gamma = (1-2\nu)/(2-2\nu)$ and ν is Poisson's ratio, $\epsilon_{zz}(\boldsymbol{x},t)$ is the vertical strain, $\Gamma(\boldsymbol{x})$ is the magnitude of initial topographic gradients of the top reservoir surface, and $H(\boldsymbol{x})$ is a poro-elastic modulus defined as $1/H = 1/H_r + 1/H_s$ where $H_r = \Delta P/\epsilon_{zz}$ which is the ratio of pore pressure change to vertical strain, and H_s is a skeletal elastic constant.

The probability of frictional failure, P_f, within an infinitesimal volume element follows as the probability of the Coulomb stress state exceeding zero, $P(C > 0)$. The rate of friction failure events with time and per unit area within some infinitesimal region may be described by a Poisson point process intensity function, λ, such that

$$\lambda(\boldsymbol{x},t) = h\left(\frac{\partial P_f}{\partial C}\right)\left(\frac{\partial C}{\partial t}\right), \tag{5}$$

where $h(\boldsymbol{x})$ is the reservoir thickness.

Under a uniform distribution of initial stresses, often associated with a large population of active fault segments at random phases within the earthquake cycle, the Poisson intensity function is simply:

$$\lambda(\boldsymbol{x},t) = h\theta_0\Delta\dot{C}, \tag{6}$$

and $\Delta\dot{C}$ is the temporal derivative of the incremental Coulomb stress, $\Delta C(\boldsymbol{x},t)$, and θ_0 is a coupling constant related to the areal density of potential failure

sites such as pre-existing fault segments. The expected areal event density, Λ, over the time interval $(0, t)$ follows as

$$\Lambda(0,t) = \int_0^t \lambda(\boldsymbol{x}, t)dt = h\theta_0 \Delta C, \tag{7}$$

which depends only on the stress change, ΔC, and not the rate of that stress change, $\Delta\dot{C}$.

For initially inactive faults, the uniform initial stress assumption is not necessarily applicable. Failures may be initially limited to the tail of the initial stress distribution which in general conforms to a Generalized Pareto distribution. Following Bourne and Oates (2017) and considering the central case of the GP distribution the Poisson intensity function changes to:

$$\lambda(\boldsymbol{x}, t) = h\theta_0\theta_1 \Delta\dot{C} e^{\theta_1 \Delta C}, \tag{8}$$

where θ_0 and θ_1 are parameters describing the location and scale of the initial stress distribution. In the limit that incremental Coulomb stress is small relative to the scale of the initial stress distribution, *i.e.* $\theta_1 \Delta C \ll 1$, this function reduces to the response for a uniform initial stress distribution previously given by (6).

As before, a key characteristic of this elastic-Coulomb system is that the expected number of events per unit area, Λ, only depends on the incremental stress, ΔC, and not the incremental stress rate, $\Delta\dot{C}$.

$$\Lambda(0,t) = h\theta_0(e^{\theta_1 \Delta C} - 1), \tag{9}$$

This means lower depletion rates only delay events rather than avoiding them. The expected response to a step-change in depletion rate is an instantaneous change in event rate in proportion to the change in depletion rate. Similarly, the expected response to harmonic variations in depletion rates is in-phase and linear such that:

$$\begin{aligned} \dot{P}(t) &= \dot{\bar{P}}(1 + \alpha_p \sin\omega t) \\ \dot{C}(t) &= \dot{\bar{C}}(1 + \alpha_c \sin\omega t) \\ \lambda(t) &= \bar{\lambda}(1 + \alpha_\lambda \sin\omega t), \end{aligned} \tag{10}$$

where ω is the angular frequency of harmonic variation with time, t, overbars denote time-averaged values over the harmonic cycle, $\alpha_c = -\alpha_p \gamma \Gamma H / H_r$, and $\alpha_\lambda = \alpha_c \exp \lambda_1 \dot{\bar{C}} t$.

In previous studies this elastic-Coulomb model was evaluated using a time series of reservoir pressure grids with a 1-year time sampling interval (Bourne and Oates, 2017; Bourne et al., 2018). We will now describe the results of

decreasing this time-sampling to a 1-week interval in order to evaluate its response to seasonal and other intra-year variability of depletion rates within the Groningen reservoir.

The unknown model parameters $\{\theta_0, \theta_1\}$ were estimated using the previously described method of Bayesian inference (Bourne and Oates, 2017) for all $M \geq 1.5$ events from 1^{st} April 1995 to 1^{st} January 2018 and the weekly reservoir pressure grids. The resulting maximum posterior probability (MAP) model, exhibits clear seasonal and longer-term variations in the 7-day average expected Poisson event rate (Figure 8a). The exponential-like increase in mean annual rates up to 2013 remains clear, but this is now also modulated with a seasonal fractional rate variation, $\alpha_\lambda = 0.35 \pm 0.05$ up to 2015 and thereafter decreases significantly to $\alpha_\lambda < 0.05$. Alternative MAP models, that will be described further in later sections, of a viscous thin-sheet with Coulomb friction faults, and an elastic thin-sheet with rate and state

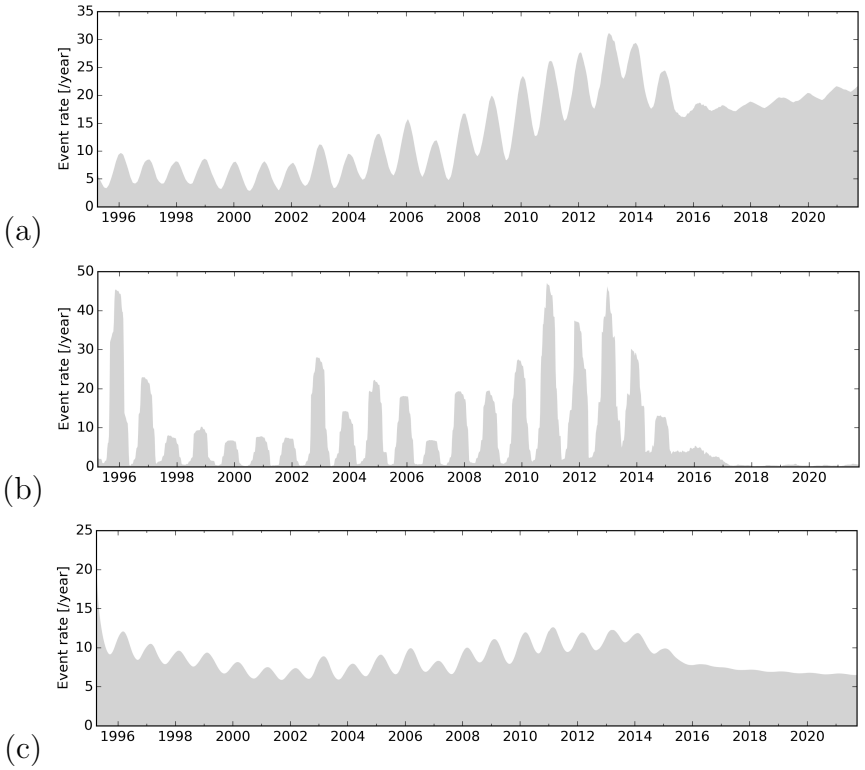

Figure 8: Temporal intensity functions for the MAP seismological model of (a) elastic and (b) viscous thin-sheet extreme threshold Coulomb failures without aftershocks, (c) elastic thin-sheet with rate and state failures under a uniform distribution of initial stresses.

friction faults show very different responses to the same pressure depletion history (Figure 8b, c).

To compare the temporal response of these models with the observed event rates some degree of additional temporal averaging is required due to the relatively small number of observed events. Such averaging involves a trade-off between temporal resolution and stochastic variability as larger time intervals reduce both the stochastic variability and the temporal resolution (Figure 9). Over a wide range of temporal averaging from 4 to 104 weeks there is credible consistency between the observed event rates and the 95% prediction interval of the MAP model for the elastic thin-sheet with coulomb friction faults excluding aftershocks. Including aftershocks does significantly improve model performance (Bourne et al., 2018), however as all these model may be extended to including aftershocks in the same manner their relative performance is not expected to be affected by this choice.

Spatial epicentral event densities under this model (Figure 10) and the time evolution of annual event density maps (Figures 11) are consistent with the observed events as previously found for the same model using a reservoir pressure grid with annual time sampling (Bourne and Oates, 2017; Bourne et al., 2018). The spatial-temporal evolution of seasonal intensity differences, $\Delta\lambda$ (Figure 12), are generally largest in the same locations as the largest intensities, λ, within the central and south-western parts of the reservoir. There is also a trend of steady seasonal amplitudes from 1995 to 2003 followed by an increasing trend until 2014, with some variability especially pronounced in 2012 and 2013 with lower amplitudes than the years before and after. By 2017, the spatial pattern changes with the largest seasonal amplitudes becoming limited to a smaller region located 10–20 km south-east of the largest seismic intensities around a cluster of production wells with some residual seasonal variation in production rates.

Within this model, the seasonal peaks in seismic intensity usually occur close to 1^{st} January each year (Figure 13), although there is some notable spatial and temporal variability about this mean behavior (Figure 14). The seasonal amplitude of the elastic-Coulomb model, $\alpha_{\lambda,sim} = 0.2$ is also broadly consistent with the observed upper bound provided by the Schuster test, $\alpha_{\lambda,obs} < 0.3$ and the month-of-year event rates (Figure 13a). All except 2 months are within the 95% model prediction interval. Of the other two months, February provides the largest exceedance of the 95% prediction interval and this is entirely due to a single large cluster of events in February 2013 (Figure 9e). For comparison, alternative MAP models of a viscous thin-sheet with Coulomb friction faults, and an elastic thin-sheet with rate and state friction faults yield higher ($\alpha_{\lambda,sim} = 0.8$) and lower ($\alpha_{\lambda,sim} = 0.1$) seasonal responses respectively (Figure 13b, c).

The annual maps of expected arrival time in peak seasonal seismic intensity (Figure 14) show a variation of ±90 days, *i.e.* from October to April. Peak seismic intensity typically occurs first in the south and later in the north driven by the time-scale for diffusion of pore-pressure away from production wells (Figure 4). There is also a complex and transient nature to this spatial-temporal distribution of arrival times reflecting the year-to-year and well-to-well variations in production rates.

Given the 289 $M \geq 1.5$ events observed over 23 years and an area of about 40 by 30 km this corresponds, on average, to one event per year per 10 by 10 km area. As such the modeled spatial temporal variability in the amplitude and arrival time of seasonal seismic intensity is too poorly sampled to be tested in detail. Instead we seek to test the field-wide amplitude and phase-lag of seasonal seismic intensity variations between 1995 and 2018. Using the Schuster p-value to measure the amplitude of seasonal event rate variations, Figure 15 compares the observed catalogue's p-value with the distribution of p-values obtained from an ensemble of 10,000 earthquake catalogues simulated according to the MAP seismological model. The observed p-value is located within the body of the simulated p-value distribution indicating good consistency between the two which are both statistically indistinguishable from a uniform random process at the 95% confidence level.

Inspection of Figure 9 shows there is no significant evidence for any large systematic time-delay between the observed and simulated seismicity rate variations. As the elastic-Coulomb seismicity model responds instantaneously to depletion rate variations there is also no evidence of significant time-delay between the observed seismicity and depletion rate variations. The possibility of aliasing of the time-delay in seasonal variations may be rejected by the lack of any significant delay in the response to the step change decreases in production rates since 2013. Nonetheless, a smaller time-delay of a few months may not necessarily be apparent in these plots due to the stochastic scatter associated with small observed event numbers. Correlograms between the time series of residual (observed minus simulated event rates) and simulated event rates provide a more sensitive and quantitative measure of smaller un-modelled time-shifts (Figure 16). These results offer no significant evidence for any non-zero time delay between any changes in the rate of local pore pressure depletion and seismic intensity.

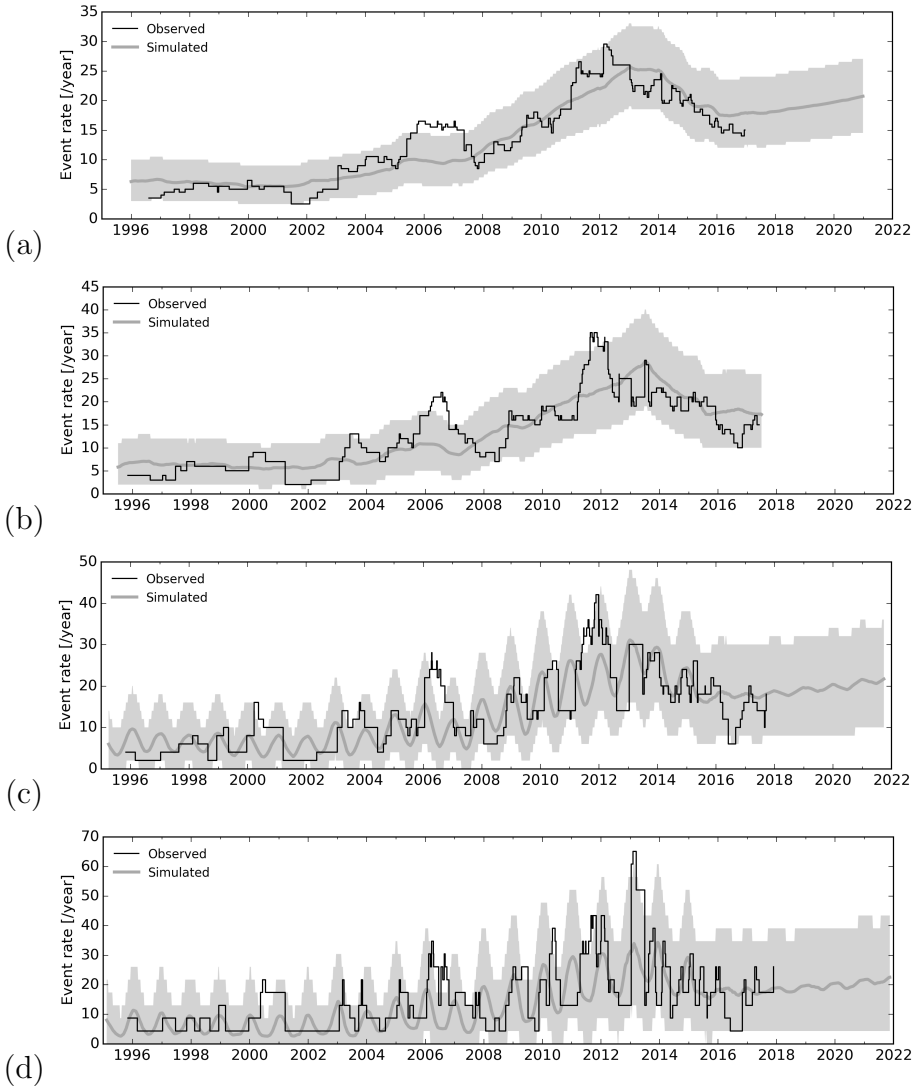

Figure 9: Expected event rates for the MAP seismological model of elastic thin-sheet extreme threshold failures without aftershocks computed as a running average over (a) 104, (b) 52, (c) 26, and (d) 12 weeks. Grey bands denote 95% prediction intervals.

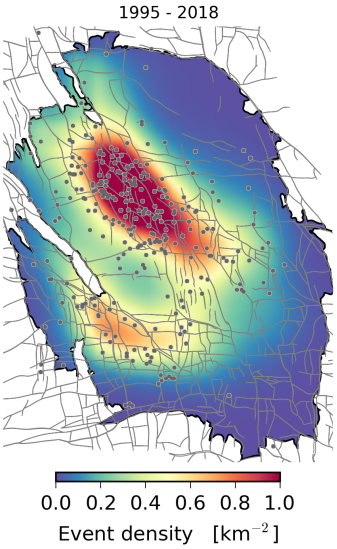

Figure 10: 1995-2018 epicentral density map for the elastic thin-sheet extreme threshold failures seismological model.

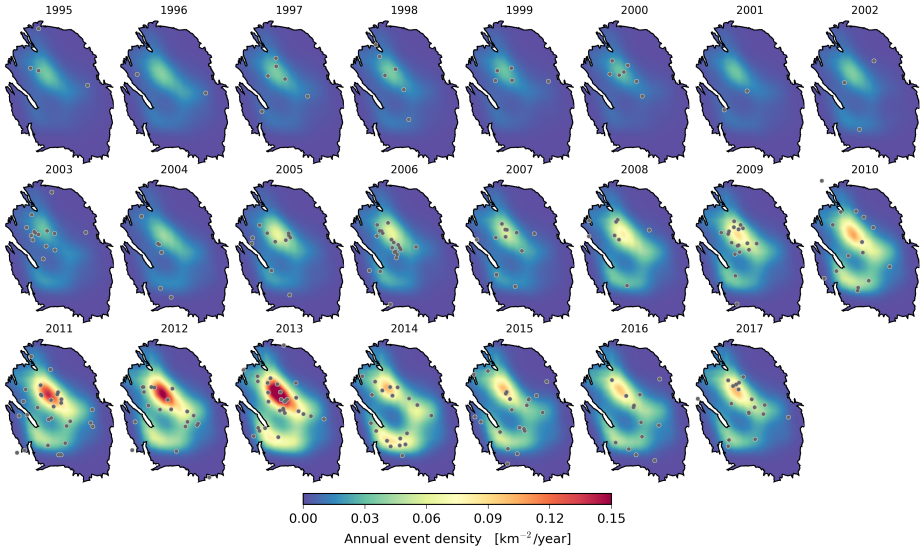

Figure 11: Annual event density maps for the elastic thin-sheet, extreme threshold Coulomb failures seismological model.

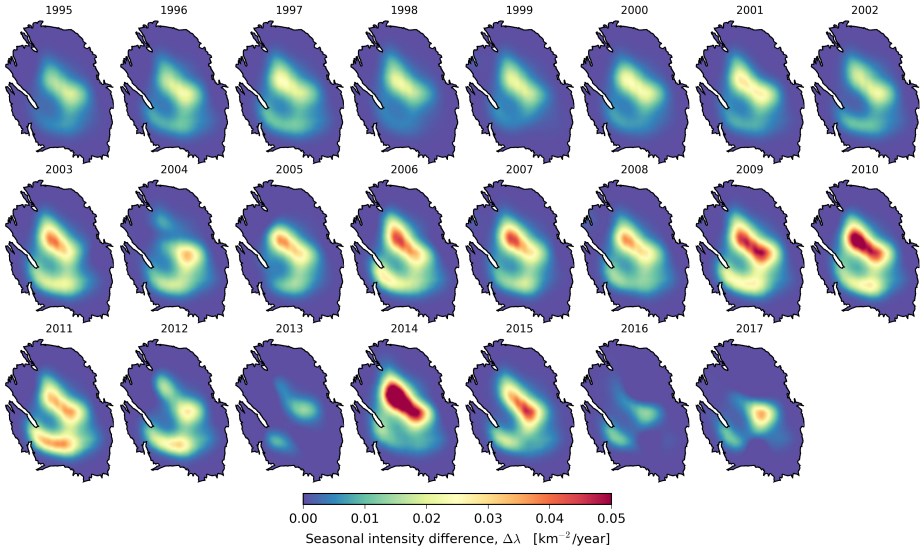

Figure 12: Seasonal amplitude of seismicity rate changes within the elastic thin-sheet extreme threshold failures seismological model. This is measured as the difference between the maximum and minimum intensity within each calendar year.

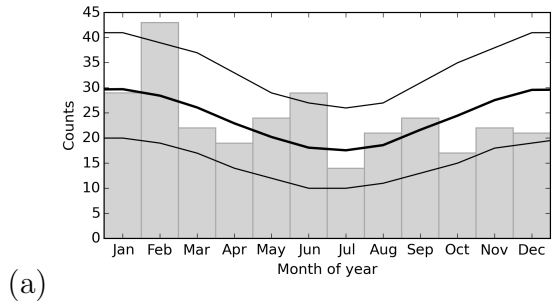

(a)

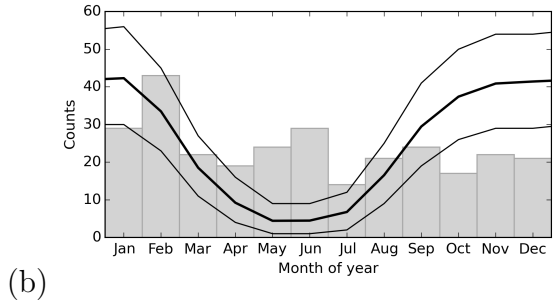

(b)

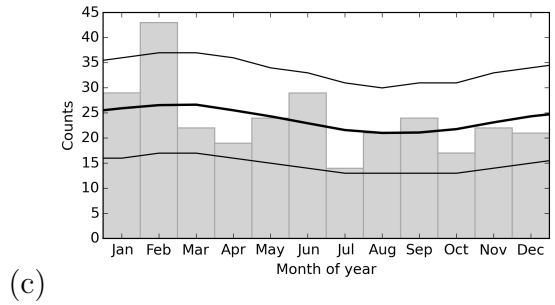

(c)

Figure 13: Mean monthly variation in observed (grey bars) and simulated (black lines) event counts for the MAP seismological model of (a) elastic and (b) viscous thin-sheet extreme threshold failures without aftershocks, and (c) elastic thin-sheet with rate and state failures under a uniform initial stress. Simulated counts are represented by their expected values and 95% prediction intervals. The relative amplitudes of seasonal variability within these two models are $\alpha_\lambda = 0.2, 0.8, 0.1$ respectively. Under the Schuster test only $\alpha_\lambda > 0.3$ is detectable with at least 95% confidence.

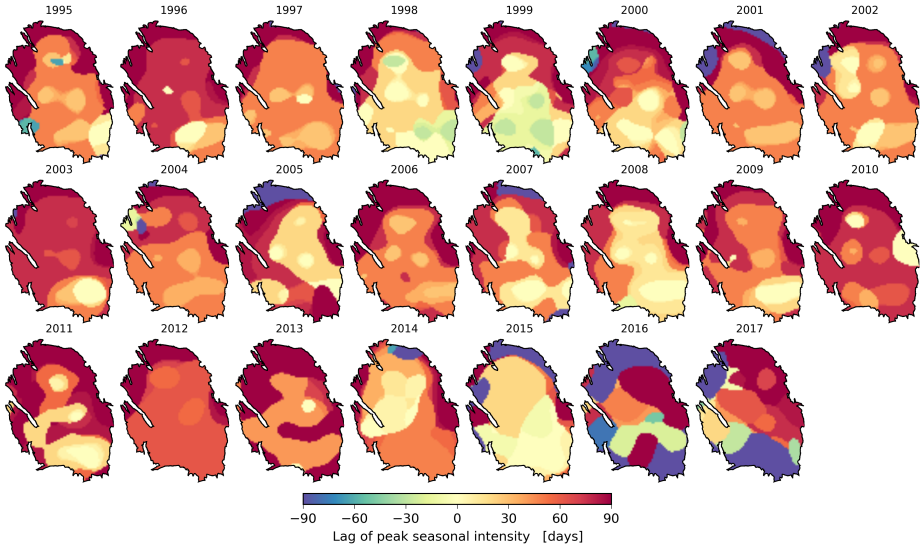

Figure 14: Lag of peak seismic intensity within the elastic thin-sheet extreme threshold failures seismological model measured relative to 1^{st} January each year varies by ±90 days. The apparent discrete time resolution of these lags is due to the 7-day sample interval of the reservoir pressure grid.

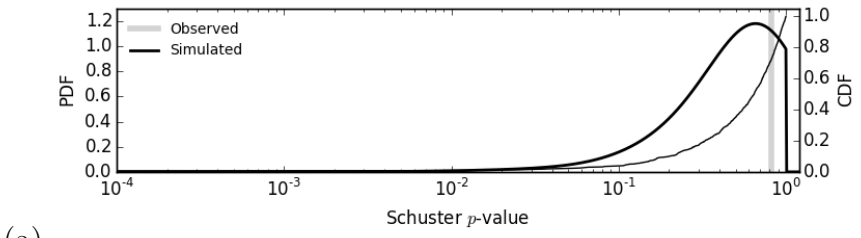

(a)

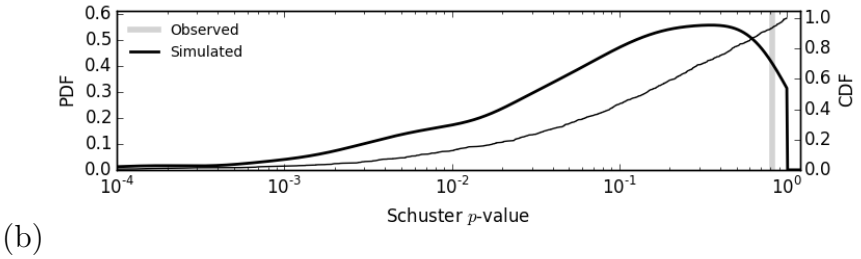

(b)

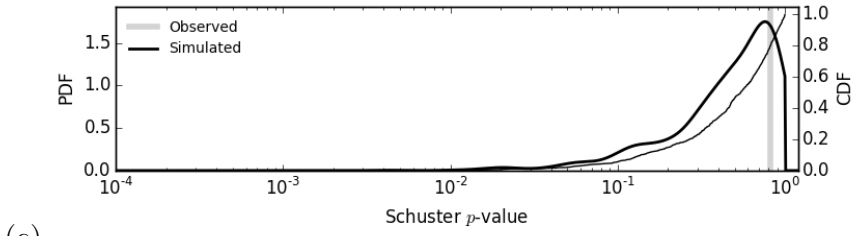

(c)

Figure 15: The distribution of Schuster p-values for simulated 1995-2018 $M \geq 1.5$ earthquakes according to the (a) elastic and (b) viscoelastic thin-sheet extreme threshold Coulomb failure models, and (c) the elastic thin-sheet model with rate and state failures under a uniform distribution of inital stresses. All three distributions exhibit large uncertainty due to the small earthquake sample size. The observed Schuster p-value corresponds to the 0.7, 0.95, and 0.8 quantiles of the simulated distributions from the three alternative seismological models respectively.

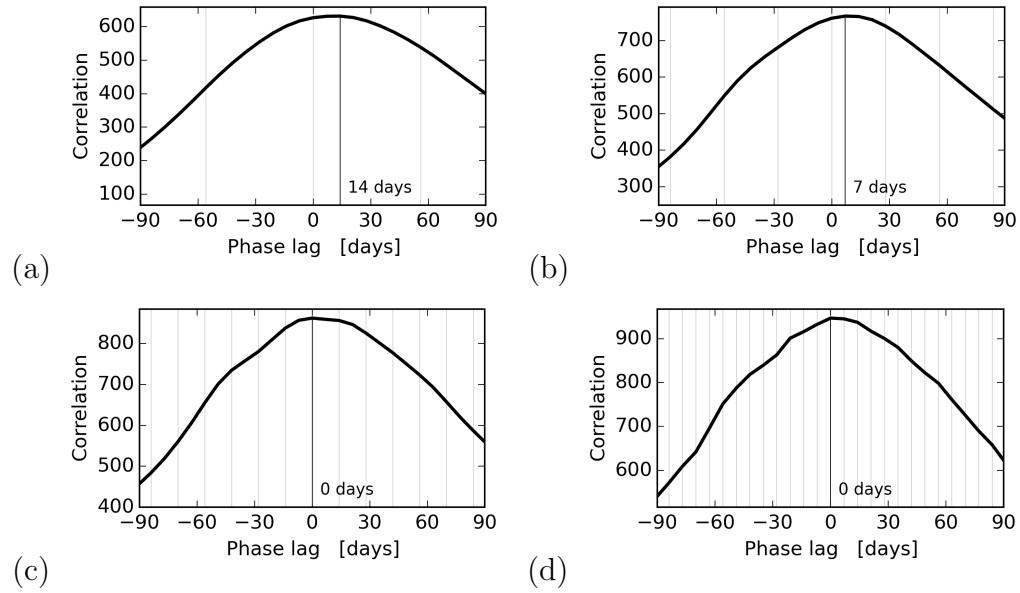

Figure 16: Correlograms of event rate residuals relative to the elastic thin-sheet Coulomb failure model which represents instantaneous stress response to pore pressure changes and instantaneous failure response to stress changes. There is no evidence for any significant time lag between pore pressure changes and induced seismicity rates, regardless of the time window for computing moving average event rates: (a) 8, (b) 4, (c) 2 weeks, and (d) 1 week.

5 Viscoelastic thin-sheet with Coulomb faults

A general linear viscoelastic model may be defined by the hereditary integral (*e.g.* Bland, 1960).

$$\epsilon(t) = \frac{\sigma(t)}{E_{i,c}} + \int_0^t K(t-t') \left(\frac{d\sigma}{dt}\right)_{t=t'} dt', \tag{11}$$

in which ϵ is the incremental strain, σ is the incremental effective stress, K is the creep function, and $E_{i,c}$ is the instantaneous creep elastic modulus. Following from this, the $t \to \infty$ steady state strain response, ϵ_{ss}, to a stress increment, $\Delta\sigma$ at constant stress rate, $\dot{\sigma}$, is

$$\epsilon_{ss} = \frac{\Delta\sigma}{E_{i,c}} + \frac{\dot{\sigma}}{\eta}, \tag{12}$$

where $1/\eta = \int_0^\infty K(t)dt$. This steady state response is simply the sum of contributions due to separate linear elastic and linear viscous deformations.

Within the linear elastic thin-sheet approximation (Bourne and Oates, 2017), incremental Coulomb stress, ΔC is linearly dependent on vertical reservoir strains, ϵ_{zz} such that $\Delta C = -\gamma\Gamma H\epsilon_{zz}$, where H is an elastic modulus, and Γ are the topographic gradients. So, by associating ϵ_{zz} with ϵ_{ss} we may express the steady state incremental Coulomb stresses within a linear viscoelastic thin-sheet as

$$\Delta C = -\gamma\Gamma H \left(\frac{\Delta\sigma}{E_{i,c}} + \frac{\dot{\sigma}}{\eta}\right). \tag{13}$$

For Coulomb fault friction, the expected number of induced earthquakes, N, is a monotonic function of ΔC. For failures within the body of a uniform initial stress distribution this takes the linear form $N = N_0\Delta C$; and for failures in the tail of some initial stress distribution this may take the exponential form $N = N_o \exp(k\Delta C)$ where N_0 and k are constants describing the tail location and shape. For such a viscoelastic reservoir, larger stress rates imply more earthquakes per unit stress increment relative to smaller stress rates. Consequently gas production at lower rates would not only delay but also avoid some earthquakes compared to the same gas production at a higher rate. A linear elastic reservoir lacks this physical freedom for aseismic stress relaxation via viscous creep processes, and so within this model lower gas production rates only delay and do not avoid earthquakes. In the large viscosity limit, $\eta \gg E_{i,c}\dot{\sigma}/\Delta\sigma$, a linear viscoelastic reservoir is identical to a linear elastic reservoir. The viscoelastic thin-sheet model is the simplest

physical generalization of the elastic thin-sheet model to incorporate aseismic creep relaxation of reservoir stresses.

Before evaluating the performance of such a viscoelastic thin-sheet extreme threshold failure model, let us first examine the transient response of a viscoelastic thin-sheet to a instantaneous step-change in stress rates (*e.g.* start of production, or any subsequent sustained change in production rates), and to harmonic variations in stress rates (*e.g.* seasonal production rate variations). The transient strain response to step change in stress rates from 0 to $\dot{\sigma}$ at time $t = 0$, depends on the creep function. Any creep function may be written as the series expansion of exponentials known as a Prony series (*e.g.* Bland, 1960) such that

$$K(t) = J_0 - \sum_{i=1}^{N} J_i \exp(-\lambda_i t), \tag{14}$$

which we now limit for simplicity to the first-order exponential creep response with characteristic rate, $\lambda = \lambda_1$. Evaluating the hereditary integral equation (11) for this case, the transient strain rate solution is simply

$$\dot{\epsilon}(t) = \dot{\sigma}\left(J_0' + J_1 e^{-\lambda t}\right), \tag{15}$$

where $J_0' = J_0 + 1/E_{i,c}$. This solution comprises both an instantaneous elastic and a transient creep response, which under the equivalence principle for linear elastic and viscoelasticity may be viewed as a time-dependent elastic modulus, $J_0 + J_1 \exp(-\lambda t)$. For the Maxwell form of the standard linear solid $J_0 = 1/E_1$, and $J_1 = E_2/(E_1 + E_2)/E_1$ (*e.g.* Bland, 1960).

For a square-pulse in stress rates, where $\dot{\sigma}(t) = \dot{\sigma}$ for $0 < t < \Delta t$ and otherwise $\dot{\sigma}(t) = 0$ (Figure 17), evaluation of hereditary integral equation (11) leads to (Appendix B)

$$\epsilon(t) = \begin{cases} \dot{\sigma}\left(J_0' t + \frac{J_1}{\lambda}(1 - e^{-\lambda t})\right) & \text{if } 0 \le t < \Delta t, \\ \dot{\sigma}\left(J_0' \Delta t + \frac{J_1}{\lambda}(e^{\lambda \Delta t} - 1)e^{-\lambda t}\right) & \text{if } t \ge \Delta t, \end{cases} \tag{16}$$

and after differentiation:

$$\dot{\epsilon}(t) = \begin{cases} \dot{\sigma}\left(J_0' + J_1 e^{-\lambda t}\right) & \text{if } 0 \le t < \Delta t, \\ \dot{\sigma}\left(J_1(1 - e^{\lambda \Delta t})e^{-\lambda t}\right) & \text{if } t \ge \Delta t. \end{cases} \tag{17}$$

There is a time-lag in the viscoelastic creep response with a characteristic time of $t_c = 1/\lambda$. According to (4) this also delays the increase in Coulomb stress relative to the depletion rates and therefore delays the associated increase in seismicity rates. In the limit $t \to \infty$, the steady state incremental

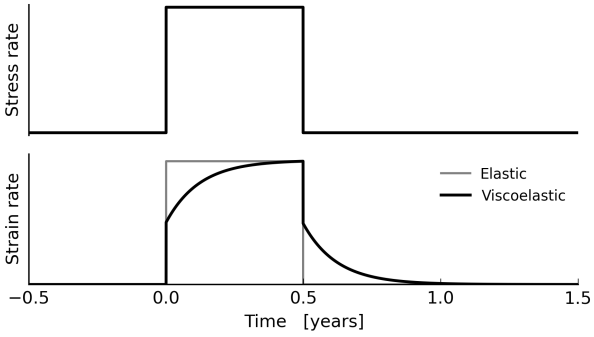

Figure 17: Strain rate responses of elastic and viscoelastic media to step-changes in stress rates.

strain is $\epsilon_{ss} = J_0'\Delta\sigma$. The ultimate incremental Coulomb stress follows as $\Delta C = -\gamma\Gamma H J_0\Delta\sigma$ which is independent of stress rate in contrast to the general case given by (13). Consequently, the ultimate expected number of induced seismic events induced depend on the incremental depletion but not the rate of that depletion.

The strain response to harmonic stress variations, $\sigma(t) = \Delta\sigma\exp(i\omega t)$, may also be obtained evaluation of the hereditary integral equation (11) (Appendix C). This yields harmonic strains of the form $\epsilon(t) = \Delta\sigma A\exp(i\omega t - i\phi)$, with time period, $T = 2\pi/\omega$, and where

$$A = \sqrt{\frac{\lambda^2 J_0'^2 + \omega^2(J_0' - J_1)^2}{\lambda^2 + \omega^2}}, \tag{18}$$

and

$$\tan\phi = -\frac{\omega\lambda J_1/J_0'}{\lambda^2 + \omega^2(1 - J_1/J_0')}. \tag{19}$$

In the low frequency limit, such that $\omega \ll \lambda$, the elastic response dominates with the amplitude and phase responses being $A = J_0'$ and $\tan\phi = 0$. In the high frequency limit, such that $\omega \gg \lambda$, the viscous creep response dominates with amplitude and phase responses of $A = J_0' - J_1$ and $\tan\phi = 0$. The largest phase shift, ϕ_c occurs at an intermediate frequency, ω_c, which follows from (18) and (19) as

$$\begin{aligned} \omega_c &= \lambda\sqrt{\frac{1}{1 - J_1/J_0'}}, \\ \tan\phi_c &= \frac{1}{2}\frac{J_1/J_0'}{\sqrt{1 - J_1/J_0'}}. \end{aligned} \tag{20}$$

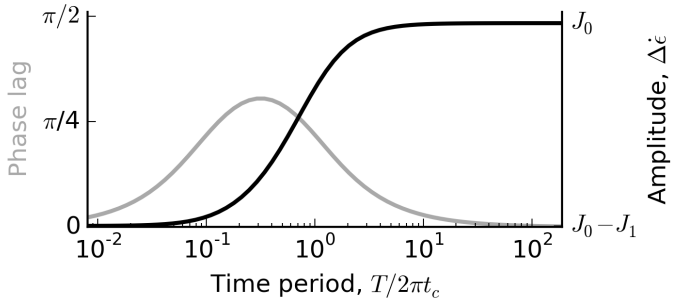

Figure 18: Spectral response of strain rates driven by harmonic stress variations within a linear viscoelastic medium, for the case $J_1 = 0.9J_0$.

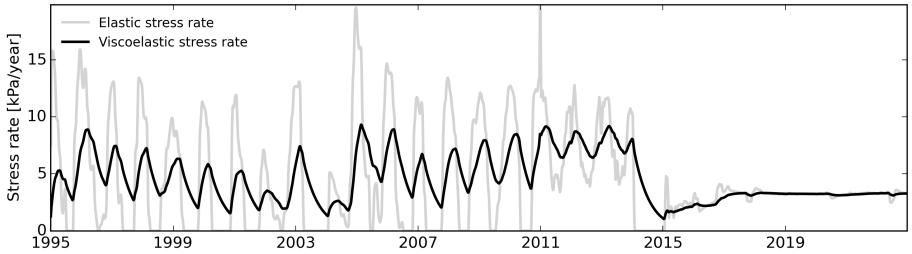

Figure 19: Coulomb stress rates for the viscoelastic thin-sheet model computed numerically according to the hereditary integral equation (11), for the case $J_1 = 0.9J_0$ at a central location (247 km, 592 km). Equivalent results for the elastic thin-sheet model are shown for comparison.

For a linear elastic system, $J_1 = 0$, strain rates vary in phase, *i.e.* $\phi = 0$, with stress rates. For a viscous dominated system, $J_1 \to J_0$, and the phase lag reaches a maximum, $\phi_c \to \pi/2$, such that strain rates are in quadrature ($\pi/2$ phase lag) with stress rates. For annual harmonic stress rate fluctuations, viscoelastic strain rates lag stress rates by 0–3 months according to the dimensionless material property J_1/J_0'.

Within the thin-sheet model, vertically-averaged reservoir strains, $\bar{\epsilon}_{zz}(\mathbf{x}, t)$, are computed according to the vertically-averaged effective stresses, $\bar{\sigma}'(\mathbf{x}, t)$, using (11) where ϵ is substituted by $\bar{\epsilon}_{zz}$, and σ by $\bar{\sigma}'_{zz}$ where $\sigma'_{zz}(t) = \sigma_{zz,i} - \alpha P(t)$. As before, the vertically-averaged Coulomb stress increment follows as $\Delta C = H\Gamma\bar{\epsilon}_{zz}$. In the Figure 19 example, peak stresses are reduced and their arrival times delayed relative to the elastic thin-sheet. This is similar to the periodic stress rate response except for additional temporal variation in amplitude. From 2015 onward, these amplitudes are significantly

diminished.

As for the elastic thin-sheet, fault failures are treated as extreme threshold failures where induced seismicity rates respond instantaneously to Coulomb stress rates and are exponentially dependent on incremental Coulomb stress. However, within the viscoelastic thin-sheet, incremental Coulomb stresses not only depend on the cumulative depletion but also the rate of depletion.

Given the evidence for no significant time delay between depletion rate and seismicity rate changes (Figure 16), we choose to consider the special case of an instantaneous creep function such that $K(t-t') = \delta(t-t')$, where δ is the Kronecker delta function. This means the hereditary integral (11) reduces to

$$\bar{\epsilon}_{zz} = \frac{\alpha}{H}\Delta P + \frac{\alpha}{\eta}\Delta\dot{P}. \tag{21}$$

. This is a simplifying assumption that reduces the computational demand by replacing a integral over depletion history with instantaneous values. In doing so we are able to better explore the solution space for optimizing the viscoelastic thin-sheet model allowing for both depletion and depletion rate effects on the Coulomb stress whilst ignoring the additional possibility of a non-zero time delay between depletion and Coulomb stress changes which seems appropriate as we currently find no evidence for any delay in seismicity rate changes relative to depletion rate changes.

Within the thin-sheet model, the incremental Coulomb stress follows as a linear combination of depletion and depletion rate such that

$$\Delta C = \gamma\Gamma H_p \left(\Delta P + \frac{H}{\eta}\Delta\dot{P}\right), \tag{22}$$

where from (Bourne and Oates, 2017, equation 15) $H_p = H/H_r$, and $H_r = \Delta P/\epsilon_{zz}$. Note all coefficients of ΔP, and $\Delta\dot{P}$ in this are non-negative.

The Poisson intensity function describing induced seismicity rates within the extreme threshold failure model then follows from substituting (22) into (8) to obtain

$$\lambda_m(\boldsymbol{x}, t) = h\theta_0\Gamma H_p(\theta_1\Delta\dot{P} + \theta_2\Delta\ddot{P})e^{\Gamma H_p(\theta_1\Delta P + \theta_2\Delta\dot{P})}, \tag{23}$$

with $\theta_1 \geq 0$ and $\theta_1 \geq 0$.

For simplicity, in this parametrisation, we treat the material ratio $H(\mathbf{x})/\eta(\mathbf{x})$ as a constant, meaning the spatial variation in $\eta(\mathbf{x})$ mirrors the inferred spatial variation in $H(\mathbf{x})$. This intensity function depends on the zero-, first- and second-order time derivatives of depletion, and the ratio of θ_2 to θ_1 describes the relative importance of viscous to elastic deformations in governing induced seismicity rates.

Viscous contributions (*i.e.* $\theta_2 > 0$) mean the expected number of events, $\Lambda(0,t)$, per unit area in the time interval $\{0,t\}$, depends on depletion and depletion rate according to the relation obtained after substituting (22) into (9):

$$\Lambda(0,t) = h\theta_0(e^{\Gamma H_p(\theta_1 \Delta P + \theta_2 \Delta \dot{P})} - 1), \tag{24}$$

given initial conditions $\Delta P(0) = \Delta \dot{P}(0) = 0$. For a viscoelastic thin-sheet, *i.e.* $\theta_2 > 0$, and a given depletion increment, ΔP, lower depletion rates means a lower number of expected events. Relative to quasi-static depletion rates ($\Delta \dot{P} = 0$), the expected number of events increases with depletion rate by approximately a factor of $e^{\gamma \Gamma H_p \theta_2 \Delta \dot{P}}$.

This instantaneous creep instance of the viscoelastic seismological model may be viewed as the product of two independent space-time maps that describe the separate elastic, $\mathcal{M}_e$, and viscous, $\mathcal{M}_v$, contributions, by rewriting (24) as

$$\begin{aligned} \Lambda(0,t) &= h\theta_0(\mathcal{M}_e \mathcal{M}_v - 1), \\ \mathcal{M}_e &= e^{\theta_1 \Gamma H_p \Delta P}, \\ \mathcal{M}_v &= e^{\theta_2 \Gamma H_p \Delta \dot{P}}. \end{aligned} \tag{25}$$

We will now proceed to show the set of optimal space-time viscous maps obtained for the Groningen field only act to degrade the history match and forecast performance of the viscoelastic seismological model.

Using the same method for Bayesian inference as before, we seek to optimize this viscoelastic thin-sheet and extreme threshold failure model parameters given the observed reservoir geometry, $\Gamma(\mathbf{x})$, depletion, $\Delta P(\mathbf{x},t)$, and vertical strain, $\epsilon_{zz}(\mathbf{x},t)$. Figures 20 and 21 show the results for the thin-sheet parameters $\{\sigma_s, r_{max}\}$ and extreme failure parameters $\{\theta_0, \theta_1, \theta_2\}$ respectively. Most notable here is the posterior marginal distribution of θ_2 indicating most acceptable history matches are found in the limit of negligible viscous-like aseismic stress relaxation ($\hat{\theta}_2 \approx 0$). Given the choice of viscoelasticity, the field data strongly favours elasticity.

We also used R-tests to compare the out-of-sample performance of a model ensemble trained on the 1995-2013 observed events, according to the distribution of model likelihoods given the 2013-2018 observed events (Figure 22). This indicates the additional degree of freedom within the viscoelastic model, θ_2, lacks any explanatory power and only serves to deteriorate the apparent forecast performance.

To understand this outcome, let us consider the space-time evolution of expected seismicity rates (25) according to the independent contributions of a viscous thin-sheet (Figures 23, 24, 25) and an elastic thin-sheet (Figures 9, 10, 11) to the combined viscoelastic thin-sheet model.

The MAP viscous thin-sheet model expects declining annual rates from 1995 to 1998 (Figure 23a, b) driven by declining production rates over this period (Figure 1) whereas steady or increasing rates are observed. The expected annual rate decline from 2013 to 2018 following decreased production rates significantly exceeds the observed decline. Over the intervening period of increasing production rates (1998 to 2013) there is a credible match to the observed rise in annual events rates. The expected amplitude of seasonal event rate variations significantly exceeds any observed seasonal variation throughout the entire period (Figures 23c, d, and 13b).

Expected epicentral densities within the MAP viscous thin-sheet model is largest in the southern region (Figure 24) where depletion rates and depletion rate variability are both largest (Figure 2), but unlike the observed epicentral density which is largest in the central region. Furthermore the model expects significant inter-year variability in spatial density (Figure 11) whereas the observed densities change only steadily from year to year.

In summary, a viscoelastic thin-sheet would offer scope for improved performance if the elastic thin-sheet model under-estimates 1995-1998 annual event rates, or over-estimates 2013-2018 annual event rates, or under-estimates seasonal rate variations, or under-estimates epicentral density in the southern half of the reservoir. However, there is no significant evidence

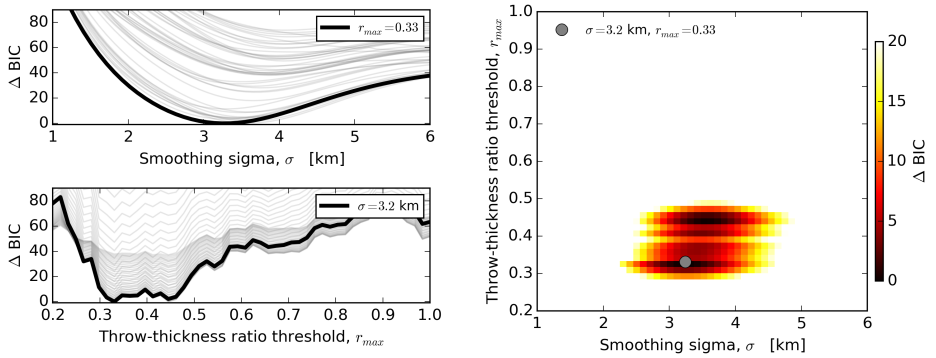

Figure 20: Grid search optimization of the viscoelastic thin-sheet stress model parameters using the extreme threshold seismological model. Results are shown for BIC statistic given the 1995-2018 $M \geq 1.5$ observed event times and epicentral locations according to model instances for the topographic gradient smoothing length-scale and maximum fault throw to reservoir thickness ratio $\{\sigma_s, r_{max}\}$. Due to the presence of the Zechstein salt formation above the reservoir, faults with larger r-values experience greater reservoir-salt juxtaposition and so greater chance of aseismic creep due to the presence of salt.

for any such bias within the elastic thin-sheet model whose most significant deficiency is to under-estimate a transient increase in event rates during 2006.

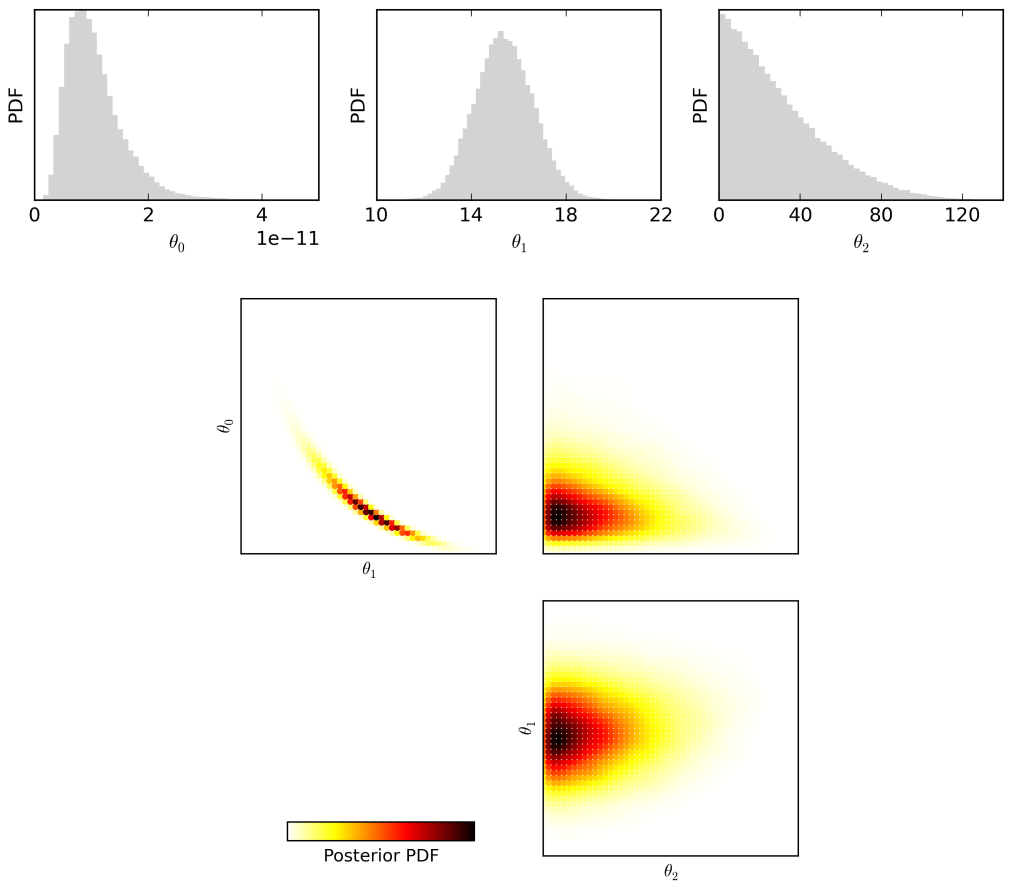

Figure 21: Marginal posterior distributions for the viscoelastic thin-sheet extreme threshold failure seismological model.

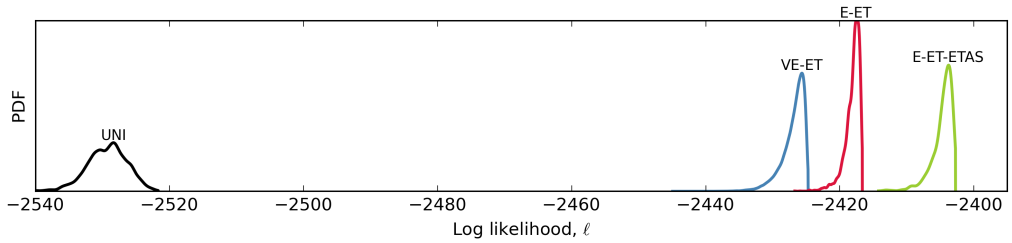

Figure 22: R-test results indicate the pseudo-prospective activity rate performance of the elastic seismological model (E-ET) significantly exceeds the alternative viscoelastic model (VE-ET) which in turn exceeds the baseline uniform model (UNI). Inclusion of aftershocks according to the ETAS model (E-ET-ETAS) yields further improvement. Each model is trained and evaluated using the 1995-2013 and 2013-2018 $M \geq 1.5$ events respectively.

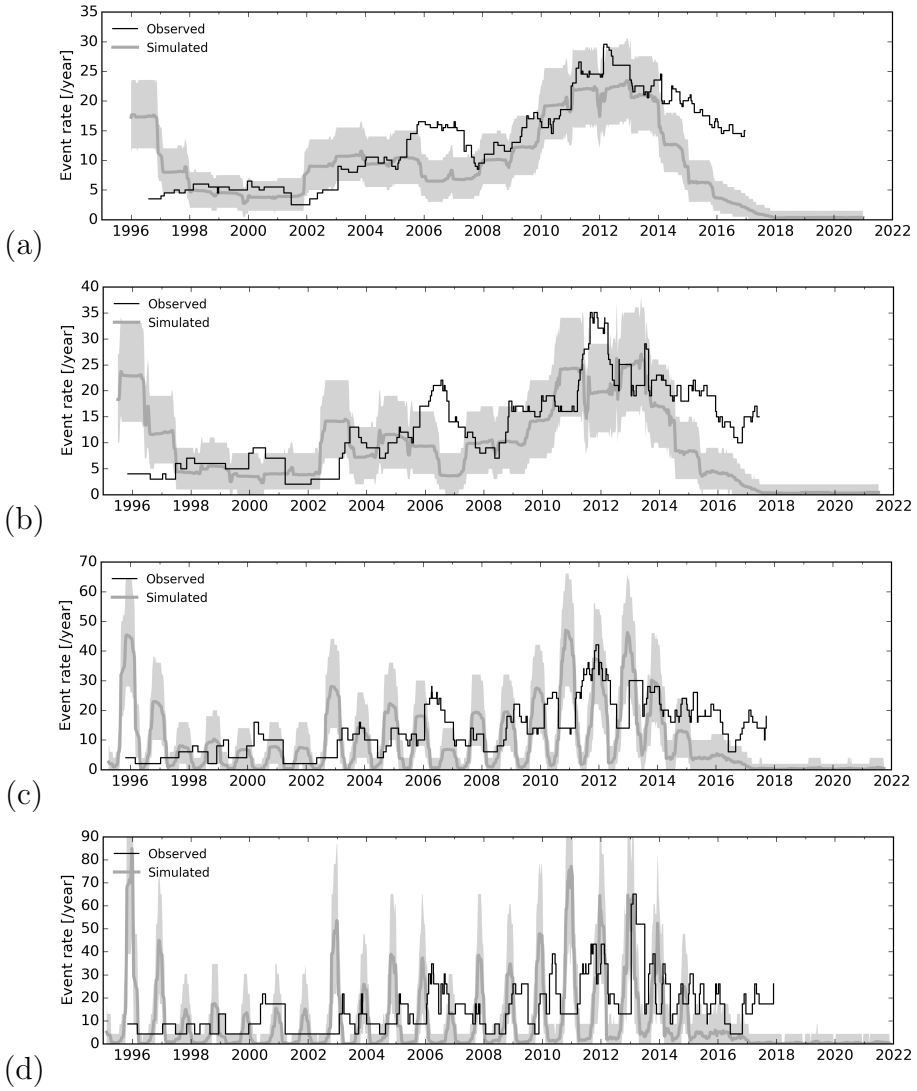

Figure 23: As Figure 9, except for the viscous thin-sheet extreme threshold failures seismological model.

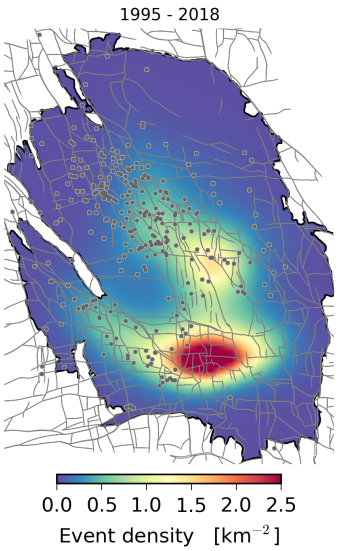

Figure 24: 1995-2018 epicentral density map for the viscous thin-sheet extreme threshold failures seismological model.

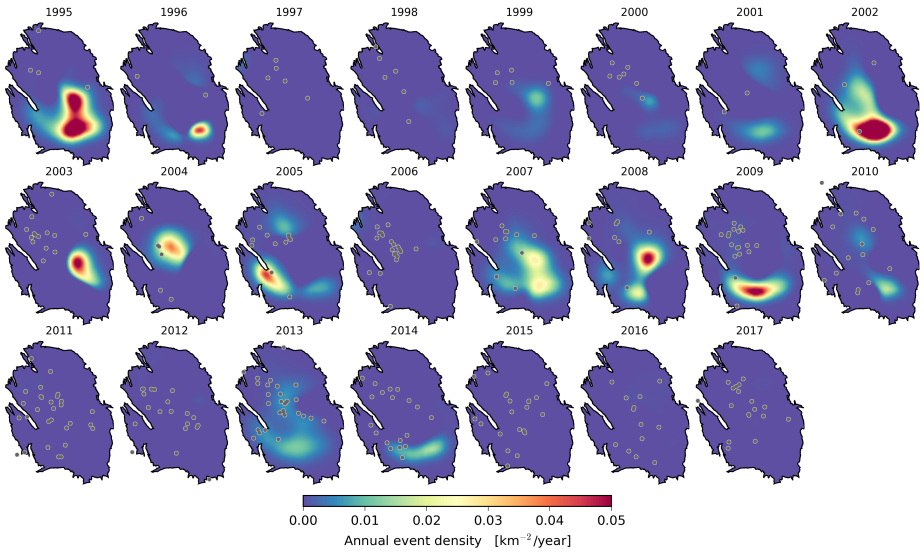

Figure 25: Annual event density maps for the viscous thin-sheet extreme threshold failures seismological model.

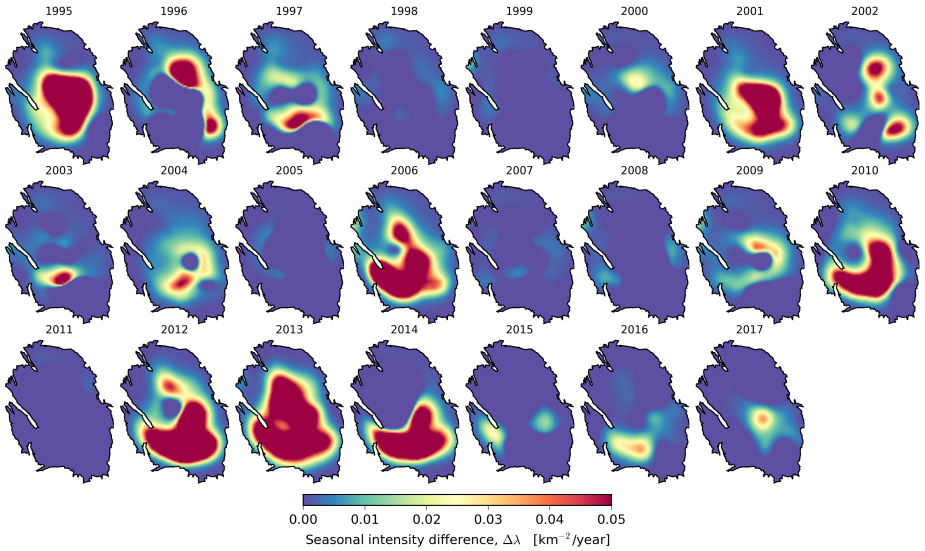

Figure 26: Annual seasonal seismicity intensity difference for the viscous thin-sheet extreme threshold failures seismological model.

6 Elastic thin-sheet with rate-and-state faults

Motivated by experimental results, the rate and state friction model includes a temporal evolution of the coefficient of friction according to a state variable that depends on slip displacement and velocity. The governing equations for the evolution of seismicity rates, R with shear stress, τ, and effective normal stress, σ, within a spring slider-block system with a uniform distribution of initial shear stresses (Dieterich, 1994) are

$$\begin{aligned} a\sigma\frac{\mathrm{d}\gamma}{\mathrm{d}t} &= 1-\gamma(t)\frac{\mathrm{d}\tau}{\mathrm{d}t}+\gamma\left(\frac{\tau}{\sigma}-\alpha\right)\frac{\mathrm{d}\sigma}{\mathrm{d}t}, \\ \frac{R(t)}{r} &= \frac{1}{\dot{\tau}_a\gamma(t)}, \end{aligned} \tag{26}$$

where $\dot{\tau}_a$ is a reference shear stress rate and r is the corresponding reference seismicity rate. Heimisson and Segall (2018) provide a clear explanation of the derivation of these equations including the underlying assumptions and limitations.

For simplicity let us first consider the limit of large normal effective stress, such that $\sigma_i \gg \Delta\sigma$, where σ_i and $\Delta\sigma$ are the initial and incremental effective normal stresses respectively. For a modified Coulomb stress, S, the system of equations reduces to:

$$\begin{aligned} S &= \tau-(\mu-\alpha)\sigma, \\ a\sigma_i\frac{\mathrm{d}\gamma}{\mathrm{d}t} &= 1-\gamma(t)\frac{\mathrm{d}S}{\mathrm{d}t}, \\ \frac{R(t)}{r} &= \frac{1}{\dot{S}_a\gamma(t)}. \end{aligned} \tag{27}$$

This is also equivalent to the particular case of constant effective normal stress, *i.e.* $d\sigma = 0$ and $dS = d\tau$. In the case of varying normal stress, a modified version of Dieterich's theory has been recently proposed (Heimisson and Segall, 2018) with equivalent behaviour for small normal stress changes and only deviates for very large changes in normal stress ($\Delta\sigma/a\sigma_i \gg -10$) yielding only slightly increased seismicity rates. Our following discussion continues with the original theory according to equations (27).

For positive stress rates, $\dot{S} > 0$, the steady state response to a constant stress rate is a constant seismicity rate, R_{ss}, in proportion to the stress rate.

$$\frac{R_{ss}}{r} = \frac{\dot{S}}{\dot{S}_a}. \tag{28}$$

This behavior is identical to the Coulomb friction model with constant values for static and dynamic coefficients of friction governing the initiation and arrest of frictional slip under a uniform distribution of initial stresses.

Following Ader et al. (2014), the system of equations (26) is solved for a general stress time history, $S(t)$, with the substitution $q(t) = e^{S(t)/a\sigma_i}$ leading to:

$$\frac{R(t)}{r} = \frac{e^{S(t)/a\sigma_i}}{1 + \frac{1}{t_a}\int_0^t e^{S(t')/a\sigma_i}\mathrm{d}t'}, \tag{29}$$

where $t_a = a\sigma_i/\dot{S}_a$ is the reference response time of the system.

For early times such that:

$$\int_0^t e^{S(t')/a\sigma_i}\mathrm{d}t' \ll t_a, \tag{30}$$

the initial transient seismicity response according to (29) is simply an exponential trend with respect to the instantaneous stress state, $S(t)$:

$$R(t) = re^{S(t)/a\sigma_i}. \tag{31}$$

Small initial stress rates, $\dot{S}_a \ll a\sigma_i$, imply $t_a \gg 1$. So for a fault system previously considered inactive, the initial exponential seismicity transient associated with any reactivation may, in principle, extend over a significant time period. Furthermore, the initial seismicity rate, r, and corresponding stress rate, $\dot{S}_a$, must be non-zero for increased seismicity rates to emerge within finite time in response to increased stress rates. So a truly inactive rate and state fault system cannot be reactived in any practical sense.

In summary, the seismicity response to given stress history, $S(t)$, depends on three rate and state model parameters: r, $a\sigma_i$, and $\dot{S}_a$. These three parameters respectively govern the initial rate, r, the characteristic response time, $a\sigma_i$, and the maximum possible, *i.e.* steady state, rate, $r\dot{S}/\dot{S}_a$.

Let us continue to consider the behaviour of this system under simple changes in stress rate or stress state. The transient system response to a single step-change in stress rates from $\dot{S}_a$ to $\dot{S}$ at $t = 0$ follows from (29) as the logistic function:

$$\frac{R(t)}{r} = \frac{K}{1 + (K-1)e^{-t/t_c}}, \tag{32}$$

where the stress rate ratio is $K = \dot{S}/\dot{S}_a$ and the characteristic time is $t_c = a\sigma_i/\dot{S}$. This represents an exponential-like transition to the new steady state seismicity rate, $\dot{S}/\dot{S}_a$, over the characteristic time-scale, t_c. For large increases in stress rate above the reference rate, such that $K \gg 1$, the initial

time evolution, $t \ll t_c \log K$, follows an exponential trend with respect to the instantaneous stress state, $S(t)$.

The expected cumulative event count, $N(t)$, follows as

$$\frac{N(t)}{r} = \int_0^t \frac{R(t')}{r} dt'. \tag{33}$$

For the stress rate step change solution (32) this evaluates to

$$\frac{N(t)}{r} = t_c K \left[\log \left(e^{t/t_c} + K - 1 \right) - \log K \right]. \tag{34}$$

In comparison, the Coulomb friction response to this same stress rate step is simply $N(t)/r = Kt$. In the limit of sufficient time, $t/t_c \gg \log(K-1)$, the ultimate number of expected events for rate and state friction differs from Coulomb friction by the constant amount:

$$\frac{\Delta N(t)}{r} = -t_c K \log K = -\frac{a\sigma_i}{\dot{S}_a} \log K. \tag{35}$$

Consequently, the delayed seismicity response under rate and state friction reduces the expected ultimate number of events in proportion to the natural logarithm of fractional increase in stress rates, but only if stress rates never decrease again.

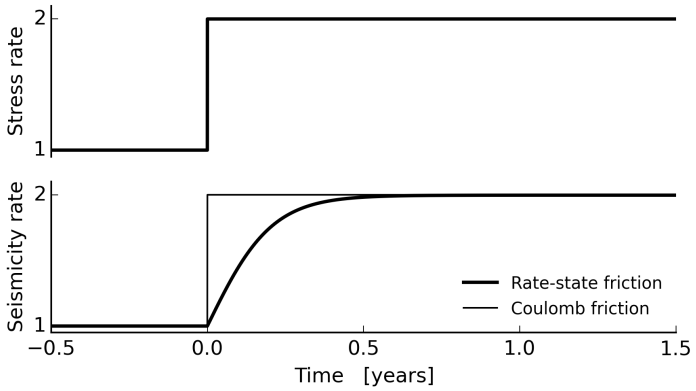

Figure 27: The transient seismicity rate response to a step-change in stress rates loading a rate-and-state fault.

Let us now extend this step-change solution to also include a subsequent equal and opposite step-change in stress rates, returning to the initial stress rates for $t \geq \Delta t$. This is of interest because it approximates the possible

seismicity response to a single seasonal cycle, or the entire life-cycle from initial to final production. Also, in the limit $\Delta t \to 0$, it represents the aftershock response to step-change in stress due to a main shock. We find the following exact solution for this box-car stress rate profile again through application of (26):

$$\frac{R(t)}{r} = \begin{cases} \frac{K}{1+(K-1)e^{-t/t_c}} & \text{if } 0 \leq t < \Delta t, \\ \frac{1}{1-Ee^{-t/t_a}} & \text{if } t \geq \Delta t, \end{cases} \tag{36}$$

where $t_a = a\sigma_i/\dot{S}_a$ is the characteristic response time at the reference stress rate,

$$E = \frac{K-1}{K}\left(e^{\Delta t/t_a} - e^{-\Delta t/t_d}\right) \tag{37}$$

and $t_d = a\sigma_i/\dot{S}_d$ is the characteristic response time for the change in stress rates such that $\dot{S}_d = \dot{S} - \dot{S}_a$. Figure 28 shows an example of this solution relative to the Coulomb friction model. Relative to the instantaneous response of the Coulomb friction model, seismicity rate changes are delayed by the non-linear transient responses to both increased and decreased stress rates.

The reduction in seismicity rates starts instantaneously with the step-down in stress rates, although the characteristic time-scale of seismicity rate reduction, t_a is larger than the response time-scale to the earlier step-up in

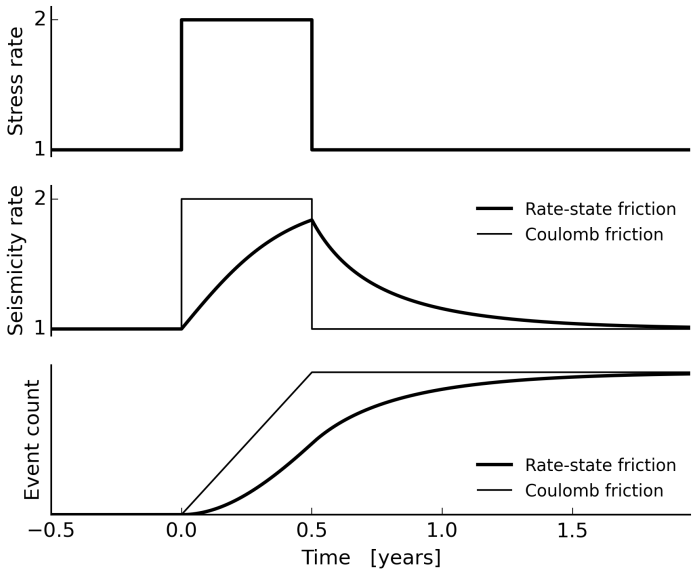

Figure 28: The transient seismicity rate response to a box-car step-up-step-down change in stress rates on a rate-and-state fault.

stress rates, t_c. This creates the asymmetric response to the stress pulse shown in Figure 28 where seismicity rates decline much more slowly than they rise. The ratio of these two response times is equal to the stress rate ratio, $t_a/t_c = K$, so this asymmetry in response times increases with the stress rate step size.

Peak seismicity rate, $R_{\max}$, occurs exactly at the end of the increased stress rate period, $t = \Delta t$, and in general depends on both the incremental stress, $\Delta S = \dot{S}\Delta t$, and the stress rate ratio, K, such that

$$\frac{R_{\max}}{r} = \frac{K}{1 + (K-1)e^{-\Delta S/a\sigma}}. \tag{38}$$

In the limit of large incremental stress, $\Delta S \gg a\sigma$, the maximum seismicity rate depends only on stress rates:

$$\frac{R_{\max}}{r} = K. \tag{39}$$

Alternatively, in the limit of small incremental stress, $\Delta S \ll a\sigma$, at large stress rates, $K \gg 1$, the maximum seismicity rate is limited by the incremental stress, ΔS, to $a\sigma_i$ ratio, or equivalently by the stress rate ratio, K and the relative time scale, $\Delta t/t_a$:

$$\frac{R_{\max}}{r} = \frac{\Delta S}{a\sigma_i} = K\frac{\Delta t}{t_a}. \tag{40}$$

This same basic control on the maximum seismicity rate will appear again when we later consider harmonic stress rate variations.

The influence of rate and state friction on the total number of events requires further consideration. For the box-car solution given by (36), the cumulative event count (33) evaluates to

$$\frac{N(t)}{r} = \begin{cases} t_a \log\left(\frac{K-1+e^{t/t_c}}{K}\right) & \text{if } 0 \le t < \Delta t, \\ t_a \log\left(\frac{K-1+e^{\Delta t/t_c}}{K}\right) + t_a \log\left(\frac{e^{t/t_a}-E}{e^{\Delta t/t_a}-E}\right) & \text{if } t \ge \Delta t. \end{cases} \tag{41}$$

The number of additional events, relative to the background seismicity rate, r, is $\Delta N(t) = N(t) - rt$. In the limit $t \to \infty$ and after some algebra, the total number of additional events due to the stress rate pulse, N_t, reduces to:

$$\frac{\Delta N_t}{r} = \dot{S}_d \Delta t = \Delta S_d. \tag{42}$$

This result is identical to the response of the Coulomb friction model to the same stress rate pulse (Figure 28). So, under rate and state friction, the

total number of events associated with the stress rate pulse only depends on the incremental stress, ΔS_d, and not the incremental stress rate, $\dot{S}_d$, or the stress history, $S(t)$. Consequently, relative to a Coulomb friction response, this rate and state frictional response acts to delay without avoiding any of the additional seismicity.

Let us now turn to the case of a step change in stress rather than stress rate. This solution may be obtained from the stress-rate box-car solution (36) in the limit $\Delta t \to 0$ and using $\dot{S} = \Delta S/\Delta t$. This means (37) reduces to $E = 1 - e^{-\Delta S/a\sigma_i}$ and (36) leads to the aftershock event rates, ΔR, above the background rate, r

$$\frac{\Delta R(t)}{r} = \frac{1}{E^{-1}e^{t/t_a} - 1}. \tag{43}$$

This suggests two limiting cases. For early times, where $t \ll t_a$, the decay in aftershock rates are

$$\frac{\Delta R(t)}{r} = \left(E^{-1} - 1 + t/(Et_a)\right)^{-1}, \tag{44}$$

which, as first noted by Dieterich (1994), is an Omori-type inverse power-law of the form, $(c + t)^{-p}$, with unit exponent, $p = 1$, and a stress change dependent characteristic time, $c = E^{-1} - 1$. For later times, such that $t \gg t_a$, aftershock rates decay exponentially as

$$\frac{\Delta R(t)}{r} = Ee^{-t/t_a} \tag{45}$$

with a time-decay constant, t_a, that is independent of the stress change, ΔS. In the limit of a small stress drop relative to the confining stress, *i.e.* $\Delta S \ll a\sigma_i$ then $\Delta S/(a\sigma)$.

From (42), the expected total number of aftershocks, N_a, depends only on the stress step size, such that $N_a = r\Delta S$.

We will now show the seismicity response to a rate and state frictional fault subject to harmonic stress rate variations exhibits the same properties of delaying without avoiding induced seismicity as previously found for box-car stress rate changes. Consider harmonic stress rate variations of the form, $\dot{S}(t) = \dot{S} + \Delta\dot{S}e^{i\omega t}$ where $\omega = 2\pi/t_p$ and t_p is the harmonic time period. Within the small perturbation approximation, $\Delta\dot{S}t \ll a\sigma_i$, the harmonic variation in seismicity rates follow from (29) as

$$\frac{R(t)}{r} = K\left(1 - \frac{\Delta\dot{S}}{\dot{S}}\frac{e^{i(\omega t+\phi)}}{\sqrt{1+\omega^2 t_c^2}}\right). \tag{46}$$

This solution is the superposition of two terms: the steady state response to the constant stress rate, $\dot{S}$, and the harmonic response to harmonic stress rates, $\Delta\dot{S}e^{i\omega t}$. The harmonic part is characterized by a phase lag, ϕ, of seismicity rates relative to the stress rates such that $\tan\phi = 1/\omega t_c$ and a harmonic amplitude equal to $\Delta K(1+\omega^2 t_c^2)^{-1/2}$, where $\Delta K = \Delta\dot{S}/\dot{S}_a$ is the harmonic amplitude of the stress rate ratios. Both the phase and amplitude response are functions of ωt_c which is the ratio of two time-scales that govern the system $2\pi(t_c/t_p)$.

The mean seismicity rate over the harmonic cycle, $0 < \omega t + \phi < 2\pi$, is simply $\bar{R} = rK$, which is independent of the frequency, ω, and the amplitude, $\Delta\dot{S}$ of the harmonic stress rate variations. This mean rate is identical to the steady state solution for a rate and state frictional fault under a constant stress rate given by (28) and also identical to the Coulomb friction fault model. Consequently neither the frequency nor the amplitude of harmonic stress variations on a rate and state frictional fault have any influence on the mean seismicity rate. The mean seismic hazard and risk will be equally insensitive the such harmonic stress variations only if the average b-value also remains unchanged. However, analysis of b-value sensitivity to harmonic stress variations is outside the scope of this analysis.

Figure 29 shows the phase and amplitude of harmonic variations in seismicity rates, where the harmonic amplitude, ΔR, is given as a fraction of the mean rate, $\bar{R}$, such that

$$\alpha_\lambda = \frac{\Delta R}{\bar{R}} = \frac{\Delta\dot{S}}{\dot{S}} \frac{1}{\sqrt{1+\omega^2 t_c^2}}. \tag{47}$$

In the low frequency limit, $t_p \gg t_c$, seismicity rates are in phase with the stress rates and attain their maximum amplitude, ΔK, which is identical to the amplitude for a Coulomb friction fault model. In the high frequency

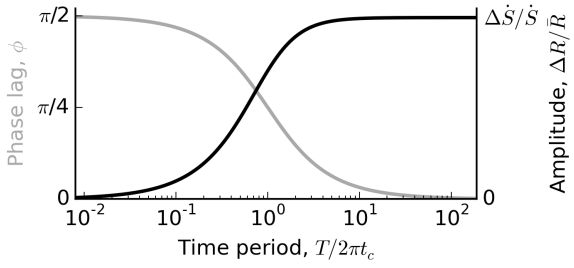

Figure 29: The phase and amplitude response of seismicity rates due to harmonic stress rates loading a rate-and-state spring slider system.

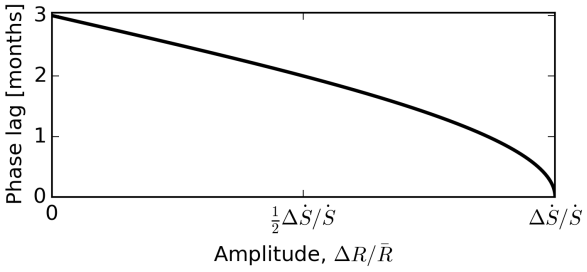

Figure 30: Phase lag as a function of amplitude response according to Figure 29 for annual harmonic stress rate variations.

limit, $t_p \ll t_c$, the seismicity rates lag stress rates in quadrature but the amplitude of variation tends to zero. In between these frequency limits, larger phase lags correspond to smaller amplitudes. For annual periodicity in shear stress rates, the maximum phase lag is 3 months, but this occurs with zero amplitude (Figure 30). Exceeding the small perturbation limit does not change these results. Example solutions in the low frequency limit obtained by numerical integration of (29) still yield harmonic variations in seismicity rate as shown in Figure 31.

Interpreting the evolution equation (29) as representing seismicity rate per unit volume, it follows that the Poisson intensity function for the number

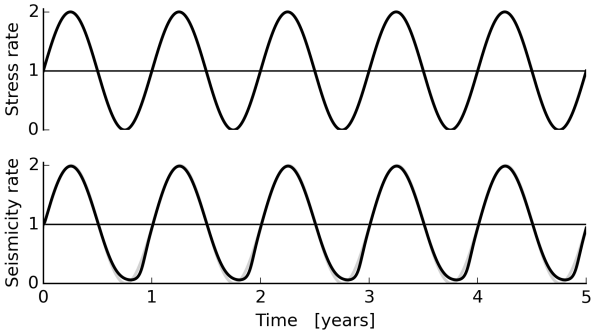

Figure 31: Example of seismicity rates due to harmonic stress rates loading a rate-and-state spring slider system (thick lines) shown in comparison to an equivalent constant stress rate (thin lines).

of events per unit time per unit area is

$$\begin{aligned}\lambda(\mathbf{x},t) &= \theta_0 h(\mathbf{x}) \frac{e^{S(\mathbf{x},t)/\theta_1}}{1+\frac{\theta_2}{\theta_1}\int_0^t e^{S(\mathbf{x},t')/\theta_1}\mathrm{d}t'}, \\ \Lambda(\mathbf{x},t) &= \int_0^t \lambda(\mathbf{x},t')\mathrm{d}t',\end{aligned} \tag{48}$$

where h is the reservoir thickness, $\theta_0 = r$ is the initial event rate per unit area, $\theta_1 = a\sigma_i$, and $\theta_2 = \dot{S}_a$ is the initial stress rate. Numerical integration of (48) for a given choice of parameter values $\{\theta_0, \theta_1, \theta_2\}$ over the complete stress time history for each grid cell of the elastic thin-sheet model of the Groningen reservoir computes the complete space-time distribution of seismic intensity. Further numerical integration over the spatial coordinates for each time sample yields the time series of expected total seismicity rates (Figure 32).

For $a\sigma_i = 0.5$ kPa, and $\dot{S}_a = 0.4$ kPa/year, the characteristic response time-scale is sufficiently small that seismicity rates are quasi-steady state (Figure 32a) and vary in proportion to stress rates according to (28). This yields a seasonal seismicity amplitude of $\alpha_\lambda = 0.2$, with peak seismicity rates which coincide with peak stress and production rates around 1977. This model instance fails to explain the delayed and exponential-like rise of seismicity rates relative to stress rates. Increasing the $a\sigma_i$ value to 5 kPa increases the seismicity response time which delays and diminishes the seasonal peaks in seismicity rate but peak seismicity still occurs around 1977 (Figure 32b).

The rate and state model is unconditionally stable at zero initial stress rates, but reducing $\dot{S}_a$ close to zero yields the possibility of multi-decade delays in the arrival time of detectable seismicity rates, with an exponential-like rise of seismicity rates with peak seismicity around 2014 when production rates and consequently stress rates were decreased (Figure 32c, d). Note that although seismicity response time-scales to the start of production and to the start of sustained production cuts in 2014 are comparable it still takes about 30 years for seismicity rates to initially increase by several orders of magnitude to become apparent consistent with the much smaller subsequent fractional decrease appearing within just a few years.

Repeating the previous thin-sheet optimization process for the elastic thin-sheet with rate and state friction faults we find similar optimal values of 3.1 km for the length-scale of spatial smoothing and a maximum fault throw to reservoir thickness ratio for seismogenic faults of 0.43 (Figure 33). The grid search resolution is less than for the viscoelastic thin-sheet due to the computational effort required to numerically evaluate (48) according to the stress history of each observed event and each reservoir grid block.

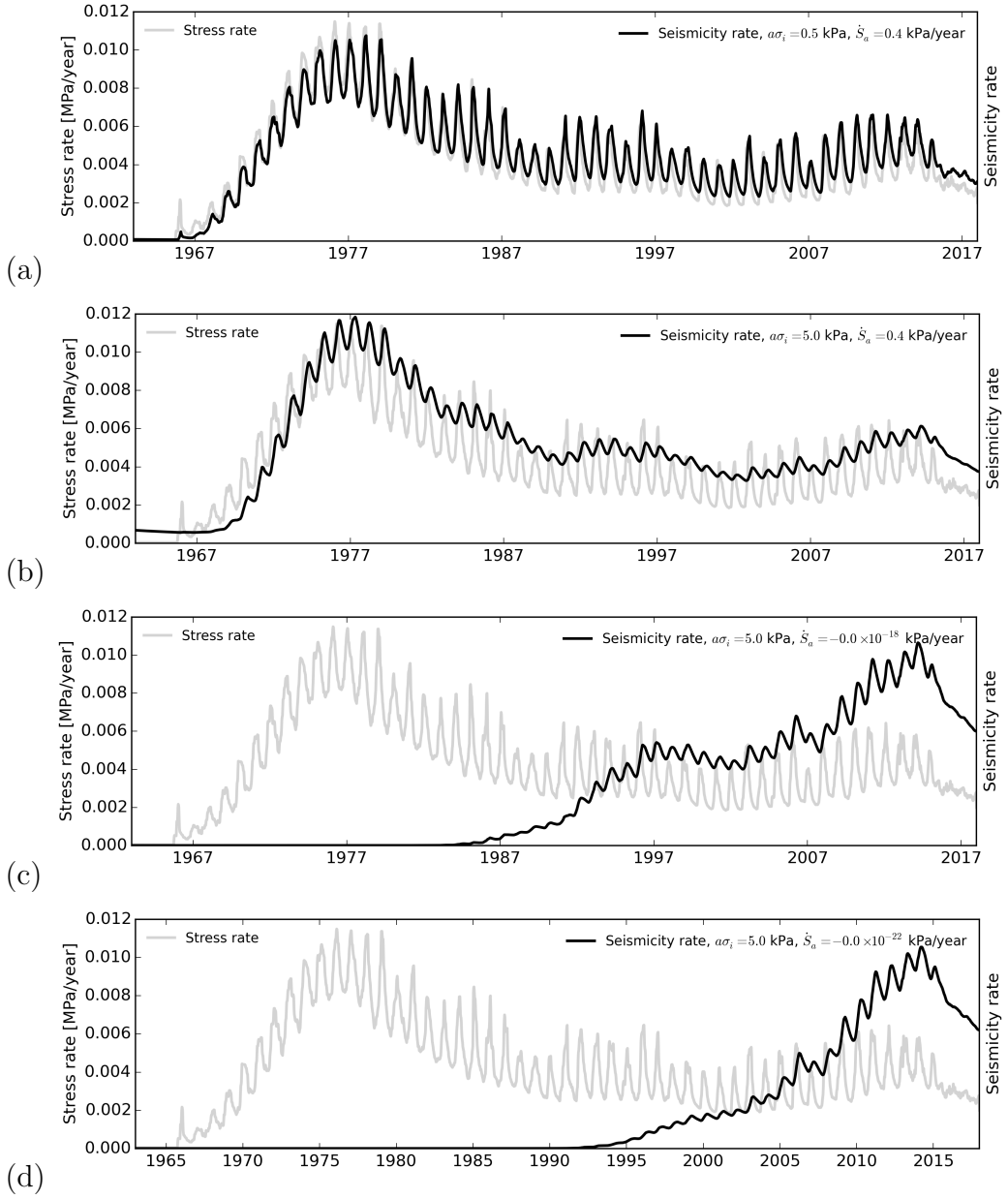

Figure 32: Total seismicity rates computed according to the rate and state fault friction model given the elastic thin-sheet model of Groningen stress time series for (a) $a\sigma_i = 0.5$ kPa, $\dot{S}_a = 0.4$ kPa/year, (b) $a\sigma_i = 5$ kPa, $\dot{S}_a = 0.4$ kPa/year, (c) $a\sigma_i = 5$ kPa, $\dot{S}_a = 10^{-18}$ kPa/year, and (d) $a\sigma_i = 5$ kPa, $\dot{S}_a = 10^{-20}$ kPa/year.

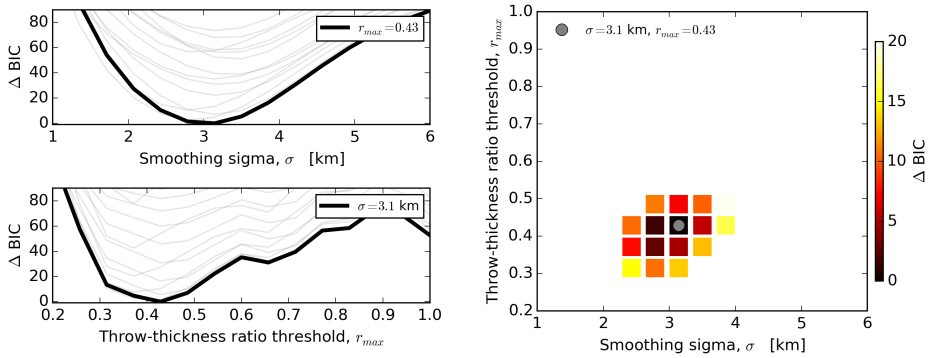

Figure 33: Grid search optimization of the elastic thin-sheet stress model using the rate and state seismological model. Results are shown for the BIC statistic given the 1995-2018 $M \geq 1.5$ observed event times and epicentral locations according to model instances for the topographic gradient smoothing length-scale and maximum fault throw to reservoir thickness ratio $\{\sigma_s, r_{max}\}$.

Figure 34 shows the posterior distribution of rate and state parameters $\{\theta_0, \theta_1, \theta_2\}$ given the observed 1995 to 2013 $M \geq 1.5$ events, stress histories inferred from the optimal elastic thin-sheet, and non-negative uniform prior distributions. Pseudo-prospective performance as measured by the R-test for 2013 to 2018 $M \geq 1.5$ events (Figure 35) indicates performance spread within the ensemble of optimized rate and state models (E-RS) significantly less than the other thin-sheet models, although significantly better than the baseline model (UNI). If the rate and state thin-sheet model is constrained to its initial exponential transient form ($\theta_2 = 0$, ET-RS2) then R-test results improve with the best performances comparable to the worst performing elastic thin sheet models (E-ET).

MAP model event rates show excellent agreement with the observed exponential-like rise in rates (Figure 36) and the spatial density of epicentres (Figures 37, 38)) from 1995 to 2014. The principal reason for this model's under-performance relative to the elastic extreme threshold model is a systematic and significant over-prediction of event rates in all locations from 2014 to 2018.

The Groningen $M \geq 1.5$ event catalogue exhibits no evidence of annual periodicity under the Schuster test. Given the size of this catalogue, the Schuster test has sufficient statistical power to detect annual periodicity with 95% confidence for fractional variations, $\alpha_\lambda > 0.3$. The MAP Coulomb fault friction seismological model yields $\alpha_\lambda = 0.2$ (Figure 13a) indicating $\Delta\dot{S}/\dot{S} = 0.2$. On the other hand, the MAP rate and state fault friction model yields $\alpha_\lambda = 0.1$ with a phase-lag of 2-3 months (Figure 13c) consistent

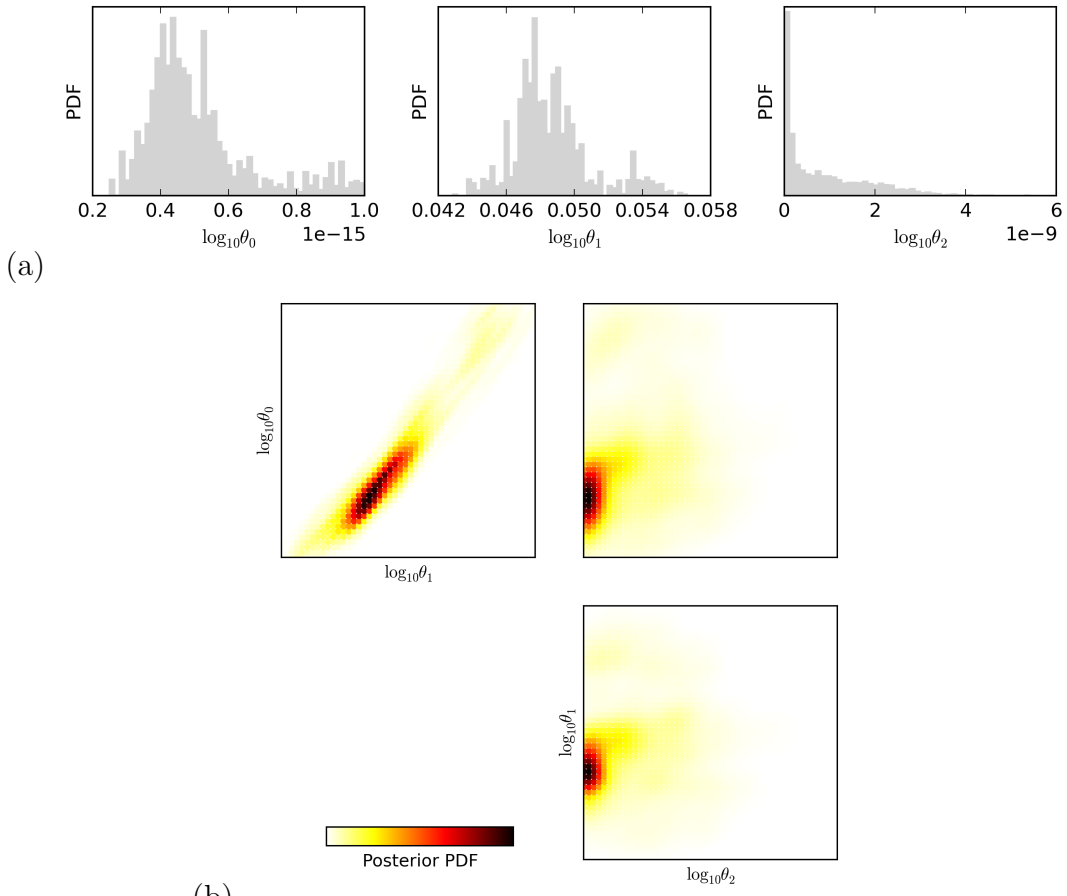

Figure 34: (a) Marginal and (b) joint posterior distributions for the elastic thin-sheet seismological model with rate and state faults under uniform initial stress.

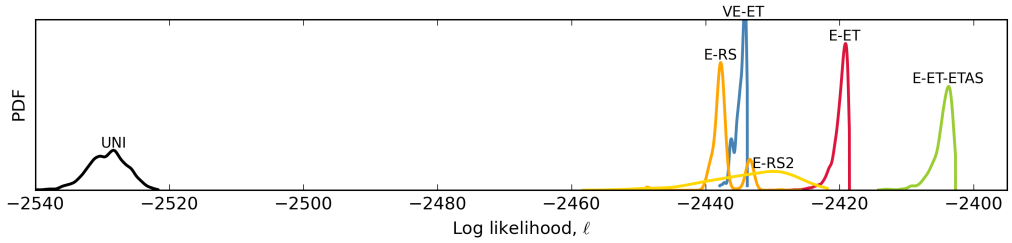

Figure 35: R-test results as previously shown in Figure 22, except with the inclusion of two results obtained for the rate and state elastic thin-sheet model.

with Figure 30.

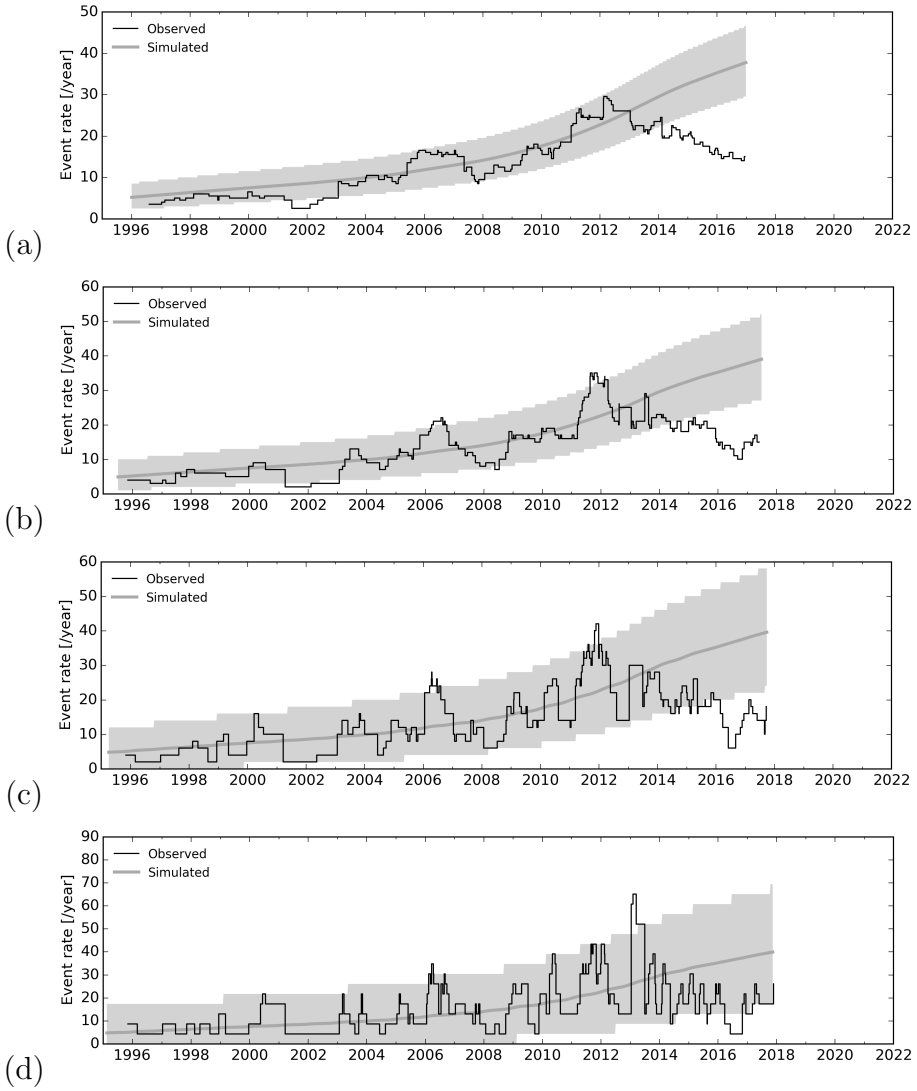

Figure 36: As Figure 9, except for the MAP elastic thin-sheet seismological model with rate and state failures under a uniform distribution of initial stresses.

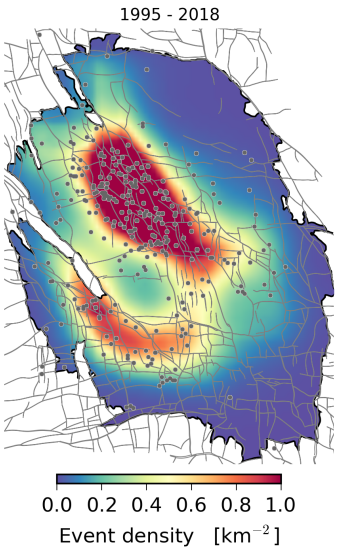

Figure 37: 1995-2018 epicentral density map for the elastic thin-sheet, rate and state failures seismological model.

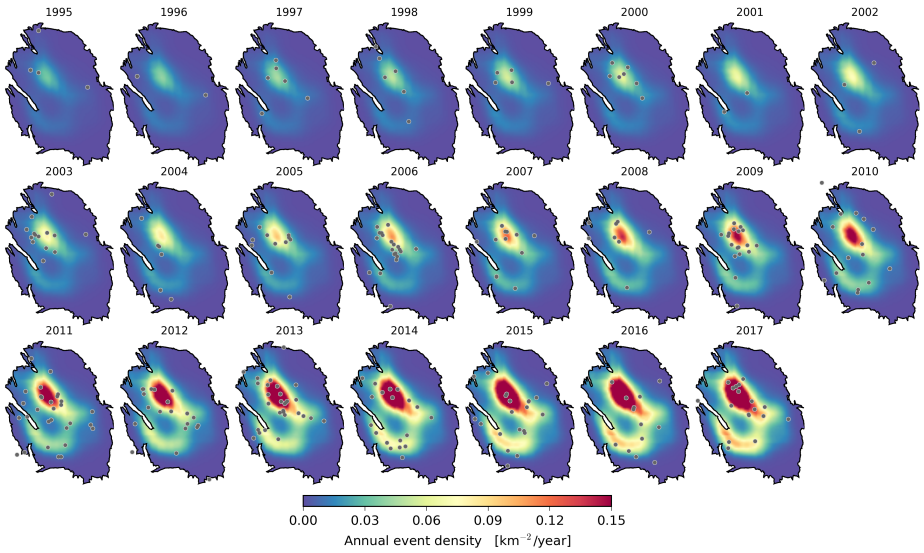

Figure 38: Annual event density maps for the elastic thin-sheet, rate and state failures seismological model.

7 Discussion and Conclusions

The rates of mean pore pressure depletion within the Groningen field were subject to significant (±50%) and systematic (from before 1995 to 2015) cyclic variations driven by seasonality in the market demand for gas production (Figure 1). As a cautionary measure in 2015, this cyclic variation was significantly reduced to $< \pm 5\%$ and sustained (2015 to 2018). Hydraulic diffusion of reservoir pore pressure changes away from the production wells induces significant seasonal variations in reservoir depletion rates albeit with decreasing amplitude (Figure 2) and increasing phase delay (Figure 4) with distance from these wells. Pore-elastic coupling induces similar variations in the rate of shear stress loading intra-reservoir faults, many of which are responsible for induced seismicity.

The frictional response of these re-activated faults to this periodic stress rate variation may induce additional earthquakes compared to the same incremental stress at constant stress rate. If so, then seasonal variation in gas production rates would increase the number of induced earthquakes per unit gas production relative to the alternative of constant gas production rates. Near elimination of significant seasonal variations in depletion rates from 2015, provides an opportunity to evaluate the susceptibility of induced earthquakes to cyclic stress rates. Moreover, throughout this period, the underlying secular trend of annual depletion rates also varied systematically; first a steady decrease from 0.3 to 0.2 MPa/year over 9 years (1995 to 2004), then a steady increase to 0.4 MPa/year over the next 8 years (2004 to 2013), followed by a faster decrease back to 0.2 MPa/year mostly within 3 years and thereafter steady (2013 to 2018). These secular rate variations, especially the recent reduction also provide opportunities to evaluate the rate sensitivity of induced seismicity within the Groningen field and the suitability of alternative seismological models to describe this process.

Previously developed seismological models for the Groningen gas field relied on a reservoir depletion grid with a time sampling of 1 year (Bourne and Oates, 2017; Bourne et al., 2018). As a consequence, the seasonal variations in pressure depletion and any implications on the induced seismicity were not resolved. Consequently the two key assumptions of an instantaneous poro-elastic reservoir stress response to pore pressure changes, and an instantaneous Coulomb fault friction response to reservoir stress changes were not fully evaluated. To address this possibility, three alternative seismological models were developed each based on a reservoir depletion grid with a 1 week sampling in order to fully resolve all seasonal variations in depletion rates over the 60 years of production to date from 1958 to 2018.

The first seismological model is a linear poro-elastic thin-sheet with Coulomb

friction faults and extreme threshold failures. This is identical to the previous model only evaluated with weekly rather than annual temporal resolution. Within this model, induced seismicity rates respond instantaneously and in direct proportion to fractional changes in depletion rates. This behavior is found to be in detailed agreement with the observed variation of induced seismicity rates in response to both seasonal and secular changes in depletion rates (Figure 9). Within this model lower depletion rates delay but do not avoid induced seismicity, such that the expected number of induced earthquakes depends on depletion independent of the rate of that depletion.

The second seismological model is a linear poro-visco-elastic thin-sheet with Coulomb friction faults and extreme threshold failures. This extends to first model to allow for visco-elastic-like stress relaxation due to aseismic creep processes within the reservoir or fault network. The amplitude and characteristic time-scale of this stress relaxation is governed by the effective viscosity to elasticity ratio. In the limit of zero viscosity this model is identical to the elastic model. With increasing viscosity, the amplitude and time-delay of seismicity response to depletion rate changes both increase in a non-linear, frequency-dependent manner (Figure 18). Visco-elasticity also means the amount of shear stress and the expected number of induced earthquakes depends jointly on the depletion and the rate of that depletion. Maximum aposteriori probability estimates for these model parameters given the observed history of reservoir depletion and seismicity from 1995 to 2018 indicate no significant role for visco-elastic stress relation. Pure viscous thin-sheet versions of this model demonstrate how viscous deformation processes are inconsistent with field observations for following main reasons. The amplitude of seasonal seismicity rate variations are significantly over-estimated (Figure 23c, d).The reduction in annual rates following reduced production rates from 2013 onward is significantly over-estimated (Figure 23a, b). The spatial location of earthquakes is predicted to be localized within the southern region of greatest depletion rate variability (Figures 24, 25) rather than as observed in the central region.

The third seismological model is a linear elastic thin-sheet with rate and state friction faults and uniform threshold failures. This extends the first model to allow for a transient, non-linear, stress rate dependent evolution of fault friction and seismicity. This provides an alternative explanation for the exponential-like rise of induced seismicity rates relative to stress rates. Within this model, harmonic stress rate variations yield harmonic seismicity rate variations. This means seasonal stress rate variations do not change the expected number of induced earthquakes. The amplitude and phase-lag of these harmonic seismicity rates depend on the frequency of stress rate variations (Figures 29). In the low-frequency limit, where stress rate time

periods greatly exceeds the characteristic friction response time, the response is equivalent to Coulomb friction with zero phase-lag and a seismicity amplitude directly proportional to stress rate amplitude. With increasing stress rate frequency the phase-lag increases whilst the seismicity rate amplitude decreases. In the high-frequency limit, the phase-lag reaches a maximum value of $\pi/2$ whilst the response amplitude becomes zero.

Viscoelastic models tends to over-estimates seismicity induced by seasonal depletion rate variations whereas rate and state fault friction models tends to under-estimate. In the limit of instantaneous response times, both models are equivalent to the elastic stress Coulomb friction model. In this limit, all three models are indistinguishable, providing identical and acceptable history-matches and equivalent seismicity forecasts. On this basis, the elastic thin-sheet Coulomb friction model remains an adequate basis for seismicity forecasting to support probabilistic seismic hazard and risk analysis within the Groningen gas field.

Acknowledgments

We gratefully acknowledge our colleagues from Nederlandse Aardolie Maatschappij, Rob van Eijs, Onno van der Wal, Jan van Elk, and Dirk Doornhof, and from Shell Global Solutions International, Stijn Bierman, Phil Jonathan, Chris Harris, and Rick Wentinck for their significant support during this study. The implementation of these seismological models made use of SciPy (Jones et al., 2001) and most of the figures were created using Matplotlib (Hunter, 2007).

References

Ader, T.J., Avouac, J.P., 2013. Detecting periodicities and declustering in earthquake catalogs using the Schuster spectrum, application to Himalayan seismicity. Earth and Planetary Science Letters 377-378, 97–105.

Ader, T.J., Lapusta, N., Avouac, J.P., Ampuero, J.P., 2014. Response of rate-and-state seismogenic faults to harmonic shear-stress perturbations. Geophysical Journal International Geophys. J. Int 198, 385–413.

Bierman, S., 2017. Seasonal variation in rates of earthquake occurrences in the Groningen field. Technical Report. Shell Global Solutions International. Amsterdam.

Bierman, S., Paleja, R., Jones, M., 2015. Statistical methodology for investigating seasonal variation in rates of earthquake occurrence in the Groningen field. Technical Report October. Shell Global Solutions International. Amsterdam.

Bierman, S., Paleja, R., Jones, M., 2016. Measuring seasonal variation in rates of earthquake occurrence in the Groningen field - Improved methodology following independent external review. Technical Report. Shell Global Solutions International. Amsterdam.

Bland, D., 1960. The theory of linear viscoelasticity. Pergamon Press, Oxford.

Bourne, S.J., Oates, S.J., 2017. Extreme threshold failures within a heterogeneous elastic thin-sheet and the spatial-temporal development of induced seismicity within the Groningen gas field. Journal of Geophysical Research: Solid Earth 122, 10,299–10,320.

Bourne, S.J., Oates, S.J., Elk, J.V., 2018. The exponential rise of induced seismicity with increasing stress levels in the Groningen gas field and its implications for controlling seismic risk. Geophysical Journal International 213, 1693–1700.

Chang, K.W., Segall, P., 2016. Injection-induced seismicity on basement faults including poroelastic stressing. Journal of Geophysical Research: Solid Earth 121, 2708–2726.

DeDontney, N., Lele, S., 2018. Impact of Production Fluctuations on Groningen Seismicity Part 1: Geomechanical Modelling using Rate of State friction. Technical Report. ExxonMobil Upstream Research Company. Houston.

Dempsey, D., Suckale, J., 2017. Physics-based forecasting of induced seismicity at Groningen, the Netherlands. Geophysical Research Letters 44, 1–26.

Dieterich, J.H., 1994. A constitutive law for the rate of earthquake production and its application to earthquake clustering. Journal of Geophysical Research 99, 2601–2618.

Dieterich, J.H., Richards-Dinger, K.B., Kroll, K.A., 2015. Modeling Injection Induced Seismicity with the PhysicsBased Earthquake Simulator RSQSim. Seismological Research Letters 86, 1102–1109.

Dost, B., Goutbeek, F., Eck, v.T., Kraaijpoel, D., 2012. Monitoring induced seismicity in the North of the Netherlands: status report 2010. Technical Report. KNMI, Scientific report WR 2012-03. de Bilt, The Netherlands.

Heaton, T.H., 1975. Tidal Triggering of Earthquakes. Geophysical Journal of the Royal Astronomical Society 43, 307–326.

Heimisson, E.R., Segall, P., 2018. Constitutive Law for Earthquake Production Based on Rate-and-State Friction: Dieterich 1994 Revisited. Journal of Geophysical Research: Solid Earth 123, 4141–4156.

Hunter, J.D., 2007. Matplotlib: A 2D graphics environment. Computing In Science & Engineering 9, 90–95.

Jones, E., Oliphant, T., Peterson, P., 2001. SciPy: Open source scientific tools for Python. http://www.scipy.org/.

Kroll, K.A., Richards-Dinger, K.B., Dieterich, J.H., 2017. Sensitivity of Induced Seismic Sequences to Rate-and-State Frictional Processes. Journal of Geophysical Research: Solid Earth 122, 10,207–10,219.

Nepveu, M., Van Thienen-Visser, K., Sijacic, D., 2016. Statistics of seismic events at the Groningen field. Bull. Earthquake Eng. 14, 3343–3362.

Park, T., Jamali-Rad, H., Oosterbosch, W., Limbeck, J., Lanz, F., Harris, C., Barbaro, E., Bisdom, K., Nevenzeel, K., 2018. Seasonality analysis for induced seismicity event rate time series within the Groningen Field. Technical Report. Shell Global Solutions International. Amsterdam.

Pijpers, F.P., 2016. A phenomenological relationship between reservoir pressure and tremor rates in Groningen. Technical Report. Statistics Netherlands.

Pijpers, F.P., 2018. Improved time resolution relationship between pressure and earthquake rates in Groningen. Technical Report. Statistics Netherlands.

Schuster, A., 1897. On Lunar and Solar Periodicities of Earthquakes. Proceedings of the Royal Society of London (1854-1905) 61, 455–465.

Segall, P., Lu, S., 2015. Injection-induced seismicity: Poroelastic and earthquake nucleation effects. Journal of Geophysical Research: Solid Earth 120, 5082–5103.

Tanaka, S., Ohtake, M., Sato, H., 2002. Evidence for tidal triggering of earthquakes as revealed from statistical analysis of global data. Journal of Geophysical Research: Solid Earth 107, ESE 1–1–ESE 1–11.

Tanaka, S., Sato, H., Matsumura, S., Ohtake, M., 2006. Tidal triggering of earthquakes in the subducting Philippine Sea plate beneath the locked zone of the plate interface in the Tokai region, Japan. Tectonophysics 417, 69–80.

Wenzel, F., 2015. Induced Seismicity Using Dieterich's Rate and State Theory and Comparison to the Critical Pressure Theory. Energy Procedia 76, 282–290.

A Detection threshold for periodic event rate variations

For a harmonic event rate variation, $R(t)$, relative to a constant background rate, r of the form

$$\frac{R(t)}{r} = 1 + \alpha \cos\left(\frac{2\pi t}{T}\right) \tag{49}$$

where α and T are the amplitude and time period of variation respectively. Ader and Avouac (2013) equation 4 provides the following expression for the Schuster p-value given a finite sample of N events from this harmonic rate distribution.

$$\langle -\ln p \rangle = 1 + \frac{N\alpha^2}{2}. \tag{50}$$

Alternatively for a uniform rate, *i.e.* $\alpha = 0$, the Schuster p-values are uniformly distributed with up to t/T independent samples where t is the time span of the event catalogue. So the expected smallest p-value is

$$p_{min} = T/t. \tag{51}$$

To distinguish a harmonic event rate from a uniform rate sampled by N events within time interval t, then measured p-value must be smaller than this minimum value by a factor corresponding to the chosen confidence level, c, such that $p < (1-c)p_{min}$. Combing this criteria with (50) and (51) leads to the following expression for the minimum detectable harmonic amplitude, α_c, with a time period of at least T:

$$\alpha_c = \frac{2}{\sqrt{N}} \sqrt{\log(t/T) - \log(1-c) - 1}. \tag{52}$$

B Derivation of visco-elastic response to a square pulse in stress rates

We start with the Prony expansion for the creep function given by (14), but limited to the first exponential term in the series, *i.e.*

$$K(t) = J_0 - J_1 e^{-\lambda t}, \tag{53}$$

and substituting this into the hereditary integral (11) to obtain

$$\epsilon(t) = J_0' \sigma(t) - J_1 \int_0^t e^{-\lambda(t-t')} \dot{\sigma}(t') dt' \tag{54}$$

For a square pulse in stress rates, $\dot{\sigma}(t) = \dot{\sigma}$ for $0 < t < \Delta t$, otherwise $\dot{\sigma} = 0$ this integral is evaluated separately for the two cases $t < \Delta t$ and $t/ge\Delta t$ as

$$\epsilon(t) = \dot{\sigma} \begin{cases} J_0' t - J_1 \int_0^t e^{-\lambda(t-t')} \dot{\sigma}(t') dt' & \text{if } 0 \le t < \Delta t, \\ J_0' \Delta t - J_1 \int_0^{\Delta t} e^{-\lambda(t-t')} \dot{\sigma}(t') dt' & \text{if } t \ge \Delta t. \end{cases} \tag{55}$$

Evaluation on these integrals yields the result

$$\epsilon(t) = \begin{cases} \dot{\sigma} \left(J_0' t + \frac{J_1}{\lambda} (1 - e^{-\lambda t}) \right) & \text{if } 0 \le t < \Delta t, \\ \dot{\sigma} \left(J_0' \Delta t + \frac{J_1}{\lambda} (e^{\lambda \Delta t} - 1) e^{-\lambda t} \right) & \text{if } t \ge \Delta t, \end{cases} \tag{56}$$

as given by (16).

C Derivation of viscoelastic strain response to a harmonic stress variations

For a harmonic stress variation of the form

$$\sigma(t) = \Delta\sigma e^{i\omega t} \tag{57}$$

Substituting (57) into (54) and evaluating the integral yields

$$\epsilon(t) = \Delta\sigma J_0' e^{i\omega t} - \Delta\sigma J_1 \frac{i\omega}{\lambda + i\omega} \left(e^{i\omega t} - e^{-\lambda t}\right). \tag{58}$$

Neglecting the initial transient associated with the $e^{-\lambda t}$ term, the stable solution for $t \gg 1/\lambda$ may be re-written as

$$\epsilon(t) = \Delta\sigma A e^{i\omega t + i\phi}, \tag{59}$$

with

$$\begin{aligned} A &= \sqrt{\frac{\lambda^2 J_0'^2 + \omega^2 (J_0' - J_1)^2}{\lambda^2 + \omega^2}}, \\ \tan\phi &= \frac{J_1 \omega \lambda}{J_0' \lambda^2 + (J_0' - J_1)\omega^2}. \end{aligned} \tag{60}$$

D Modified rate and state seismicity response to a stress rate pulse

Heimisson and Segall (2018) revisited the theoretical development of the Dieterich (1994) rate and state seismicity model and proposed the following modified version with a different dependence on the normal stress, $\sigma(t)$ for the expected number, N, and rate, R, of earthquakes.

$$\frac{N(t)}{r} = t_a \log\left(1 + \frac{1}{t_a}\int_0^t K(t')\mathrm{d}t'\right), \tag{61}$$

$$\frac{R(t)}{r} = \frac{K(t)}{1 + \frac{1}{t_a}\int_0^t K(t')\mathrm{d}t'}, \tag{62}$$

where

$$K(t) = \exp\left(\frac{\tau(t)}{a\sigma(t)} - \frac{\tau_i}{a\sigma_i}\right)\left(\frac{\sigma(t)}{\sigma_i}\right)^{\frac{\alpha}{a}}, \tag{63}$$

and τ_i, and σ_i are the initial shear and normal stresses respectively.

The original theory given by (27) and (29) follows the same seismicity rate equation (62) except the integration kernel, $K(t)$ is defined in terms of a modified Coulomb stress, $S(t) = \tau(t) - (\mu - \alpha)\sigma(t)$, such that

$$K(t) = \exp\left(\frac{S(t)}{a\sigma_i}\right). \tag{64}$$

These two forms clearly differ in general, but are identical in the limit of small normal stress perturbations Heimisson and Segall (2018). This can be seen by substituting $\tau(t) = \tau_i + \Delta\tau(t)$ and $\sigma(t) = \sigma_i + \Delta\sigma(t)$ into 63 to obtain:

$$K(t) = \exp\left(\frac{\Delta\tau\sigma_i - \tau_i\Delta\sigma}{a\sigma_i(\sigma_i + \Delta\sigma)}\right)\left(1 + \frac{\Delta\sigma}{\sigma_i}\right)^{\frac{\alpha}{a}}. \tag{65}$$

First-order Taylor expansion in $\Delta\sigma$ leads to

$$K(t) \approx \exp\left(\frac{\Delta\tau - (\mu - \alpha)\Delta\sigma}{a\sigma_i}\right) \approx \exp\left(\frac{\Delta S}{a\sigma_i}\right), \tag{66}$$

which is identical to (64) for $S(t = 0) = 0$.

Under the modified theory, an exact analytic solution may still be found for an arbitrarily large jump in effective normal stress from σ_i to σ at $t = 0$, whilst the shear stress rate remains unchanged such that $\dot{\tau} = \dot{\tau}_a$. This means $K(t)$ may be written as

$$K(t) = \lambda e^{\dot{\tau}_a t/a\sigma}\left(\frac{\sigma}{\sigma_i}\right)^{\frac{\alpha}{a}}, \tag{67}$$

where

$$\lambda = \exp\left(\frac{\tau_i}{\sigma} - \frac{\tau_i}{\sigma_i}\right). \tag{68}$$

Substituting this expression into (62) leads to the seismicity rate function

$$\frac{R(t)}{r} = \frac{\lambda e^{\dot{\tau}_a t/a\sigma}\left(\frac{\sigma}{\sigma_i}\right)^{\frac{\alpha}{a}}}{1 + \lambda e^{\dot{\tau}_a t/a\sigma}\left(\frac{\sigma}{\sigma_i}\right)^{\frac{\alpha}{a}+1}}. \tag{69}$$

In the limit $t \to \infty$, the resulting steady state rate, R_{ss}, is simply

$$\frac{R_{ss}}{r} = \frac{\sigma_i}{\sigma}, \tag{70}$$

indicating steady-state seismicity rates are inversely proportional to the effective normal stress.

Numerical integration of (62) for square rate pulses in the effective normal stress and shear stress yield seismicity rate solutions that differ simply by a scale factor for a wide range of effective normal stress rates (Figure 39). Peak seismicity rates increase with decreasing effective normal stress as expected (Figure 40). However, the sensitivity to increasing effective normal stress is minor compared to decreasing effective normal stress.

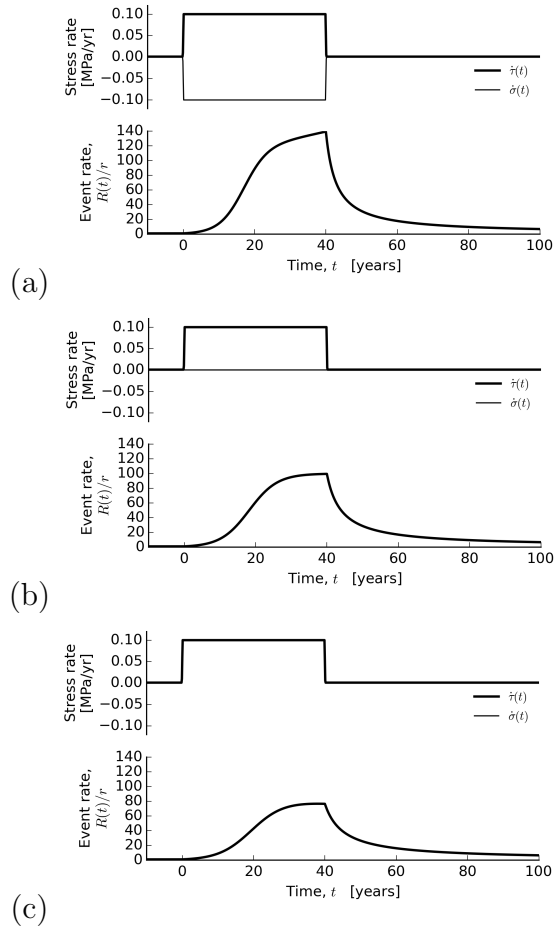

Figure 39: Seismicity rate solutions for box-car time distributions of stress rates obtained by numerical integration of (62). Results are shown for (a) $\dot{\sigma}/\dot{\tau} = -0.1$, (a) $\dot{\sigma}/\dot{\tau} = 0.0$, (a) $\dot{\sigma}/\dot{\tau} = 0.1$.

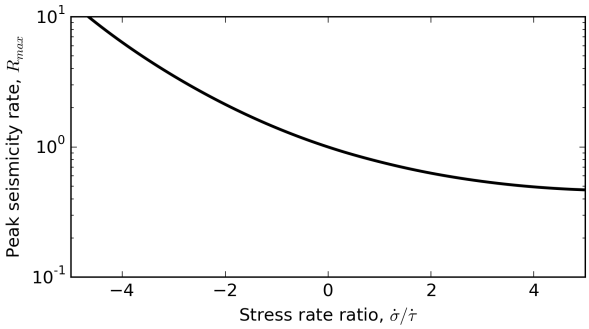

Figure 40: As Figure 39, except for peak seismicity rates as a function of $\dot{sigma}/\dot{\tau}$. Seismicity rates are normalized such that $R_{max} = 1$ for $\dot{\sigma} = 0$.

E Equivalence of seismological models

The visco-elastic thin-sheet seismological model is equivalent to the elastic thin-sheet seismological model in limit of zero viscosity which means instantaneous response times to stress perturbations.

Rate and state seismological model is equivalent to the Coulomb seismological model are equivalent in the limit of a constant stress rate. Consider the initial evolution of seismicity due to the history normal stress, $\sigma(t)$ and shear stress, $\tau(t)$, acting on a pre-existing fault plane element. The Extreme Threshold and Rate and State seismicity models are governed by the incremental Coulomb stress, $\Delta C(t)$, and the modified incremental Coulomb stress, $S(t)$ histories respectively. The associated Poisson intensity functions are respectively:

$$\begin{aligned} \lambda_{\mathrm{et}} &= \rho h \Delta\dot{C}\theta_0\theta_1 e^{\theta_1 \Delta C}, \\ \lambda_{\mathrm{re}} &= \rho h r e^{S/a\sigma_i}. \end{aligned} \tag{71}$$

These two models are identical if

$$\begin{aligned} \mu_{\mathrm{rs}} - \alpha &= \mu_{\mathrm{et}}, \\ a\sigma_i &= 1/\theta_1, \\ r &= \theta_0\theta_1\Delta\dot{C} \end{aligned} \tag{72}$$

so that the rate and state parameters (left side) match the extreme threshold parameters (right side). As the matching value of r depends on the stress rate, $\Delta\dot{C}$, these two models are only equivalent for a single constant stress rate. Consequently, the models' responses to stress rate variations will differ.

Elastic thin-sheet stress rate variations due to reservoir pore pressure changes are described by (4) which in combination with (71) and (72) mean

$$\frac{\lambda_{\mathrm{et}}}{\lambda_{\mathrm{re}}} = \gamma\Gamma H. \tag{73}$$

This means within the elastic thin-sheet stress model, the extreme threshold and rate state failure models yield identical temporal distributions, but different spatial distributions of seismicity. The modeled spatial densities are different by a scalar map, $\gamma\Gamma H$, that encodes the influence of geometric and elastic heterogeneities.

F Discretisation approximation

Consider two infinitesimal regions with stress histories, $S_1(t)$ and $S_2(t)$ in the limit of early time evolution of the rate and state seismicity model as described by (30) and (31). In order to investigate under what conditions the total seismicity rate is properly described by the mean stress history, $\bar{S} = (S_1 + S_2)/2$, let $S_1 = \bar{S} + \Delta S$ and $S_2 = \bar{S} - \Delta S$ where $\Delta S = (S_1 - S_2)/2$. The mean seismicity rate of these two regions follows as

$$R(t) = re^{\bar{S(t)}/a\sigma_i} \left(e^{\Delta S(t)/a\sigma_i} + e^{-\Delta S(t)/a\sigma_i}\right)/2. \tag{74}$$

In the limit of a sufficiently small difference in the stress histories such that, $\Delta S(t) \ll a\sigma_i$, then via Taylor expansion this expression simplifies to

$$R(t) = re^{\bar{S(t)}/a\sigma_i}. \tag{75}$$

This is identical to the rate expected if both regions experience the same mean stress history, *i.e.* $\Delta S(t) = 0$. Consequently two regions may combined and represented by their mean stress history, $\bar{S}(t)$, if $\Delta S(t) \ll a\sigma_i$.